The Mystery of the σ-Bump
A new Signature for Major Mergers?

Anna T. P. Schauer

München 2014

The Mystery of the σ-Bump
A new Signature for Major Mergers?

Anna T. P. Schauer

Dissertation
an der Fakultät für Physik
der Ludwig–Maximilians–Universität
München

vorgelegt von
Anna T. P. Schauer
aus München

München, den 29.08.2014

Advisor: Prof. Andreas Burkert
Supervisor: Rhea-Silvia Remus

Contents

List of Figures

List of Tables

1 The Formation of Early-Type Galaxies

Mass in the Universe is not uniformly distributed at small scales, but instead bound in different structures. Galaxies are among the biggest building blocks of the Universe, containing up to 10^{14} solar masses.

Galaxies exist in a big variety, from small, irregular ones with 10^7 solar masses to bright ellipticals in the centers of galaxy clusters with up to 10^{14} solar masses. The galaxies we see today have first been classified by Hubble (Hubble, 1936). In the 'Hubble turning-fork'

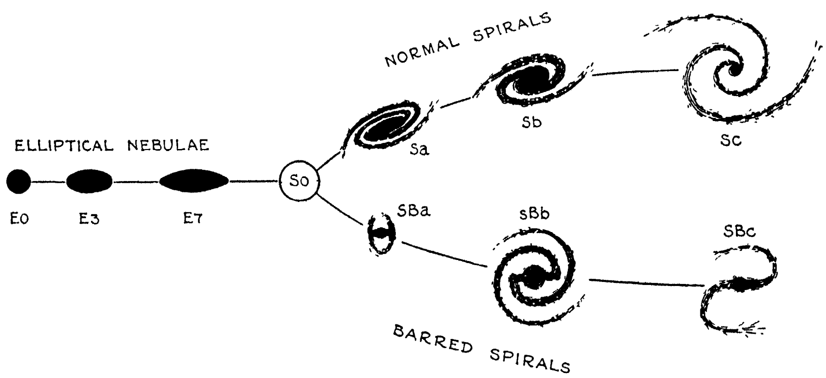

Figure 1.1: The Hubble turning fork diagram, a first classification of galaxies into spiral, S0 and elliptical galaxies. Figure taken from Hubble (1936), Figure 1.

shown in Figure 1.1, galaxies are distinguished in 'early-type' (left side of the diagram) and 'late-type' (right side of the diagram) galaxies. 'Early-types' contain elliptical galaxies with ellipticity $\epsilon = 1 - b/a$ defined via the semimajor axis a and the semiminor axis b as well as S0 galaxies, round flat galaxies with a bulge and no spiral structure. 'Late-types' are spiral galaxies, either normal ones or with a bar. Early-type galaxies have smooth surface brightnesses, are old and therefore host a red star population, whereas spiral and spiral-barred galaxies show structures like spiral arms, sometimes a bar and host a young, blue stellar population. Irregular galaxies do not have a well defined structure and include all other galaxies. Although late-type galaxies are more numerous, early-type galaxies contain more mass, see e.g. Figure 1.2.

The formation of early-type galaxies is subject of an ongoing debate in the literature. Possible formation scenarios are collisions of two spiral galaxies of similar mass (major merger scenario) or accretion of many satellite galaxies (minor merger scenario). Both types of mergers do indeed occur, for example Lambas et al. (2012) show in a galaxy-pair

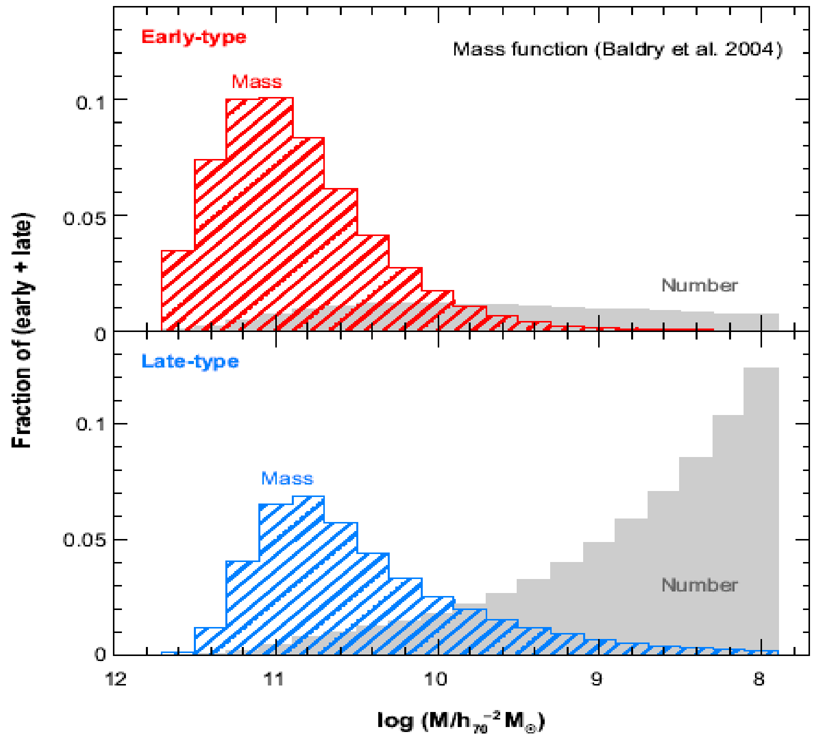

Figure 1.2: Mass and number distribution for early- and late-type galaxies. Figure taken from Renzini (2006), Figure 2.

survey that 10% of their galaxy pairs are undergoing a merger, 30% show tidal features and only 60% are undisturbed. In Figure 1.3 one can see a small gallery of currently merging galaxies.

The idea of ellipticals being formed by major mergers was first tested with numerical simulations by Toomre & Toomre (1972). In their paper, 'Galactic bridged and tails', they investigate mergers of testparticles disks on parabolic orbits and compare them to observed merging galaxies.

A famous example of merging galaxies are the antennae galaxies, shown in Figure 1.4. In this image, one can see the long tails of the merging galaxies, the starburst in the center. Toomre & Toomre (1972) were among the first to run computer simulations of galaxy collisions and to compare their major merger simulations to this observation. Figure 1.5 shows that these simulations can indeed reproduce the observed merger by a 1:1 merger with inclination angles of 60° and pericenter arguments of 30°. This is a further example how two spiral galaxies can merge into one early-type galaxy. From observations, one can see only a snapshot in the middle of the merging process, with simulations, one can reproduce the conditions and determine the final stage, an elliptical galaxy.

Other stages of merging galaxies are e.g. studied by Lambas et al. (2012). From the Slone Digital Sky Survey, they choose galaxy pairs and attribute them to be merging,

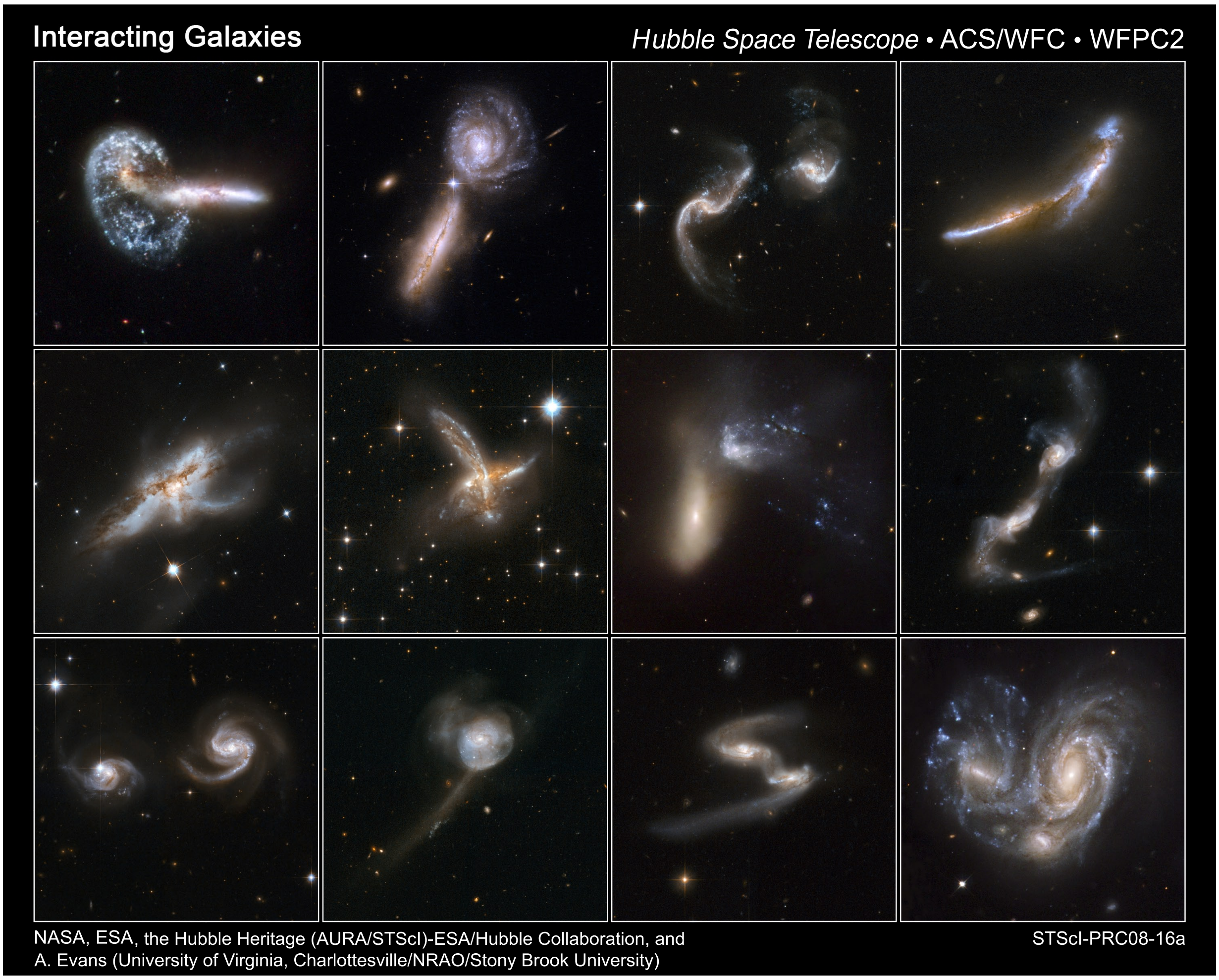

Figure 1.3: Gallery of merging galaxies. Credit: NASA, ESA, the Hubble Heritage (STScI/AURA)-ESA/Hubble Collaboration, and A. Evans (University of Virginia, Charlottesville/NRAO/Stony Brook University).

having a tidal feature or being not disturbed. In Figure 1.6, one can see these three stages.

Recent observations have shown that there exists a large variety of elliptical galaxies with a similar shape, but different kinematics (see e.g. Emsellem et al. 2011; Krajnović et al. 2011). Therefore, the classification of elliptical and S0 galaxies is currently being replaced by distinguishing fast and slow rotating early-type galaxies, partly with kinematically distinct cores.

The distinction between slow and fast rotating galaxies can be obtained by an ϵ-λ_R diagram. λ_R (Emsellem et al., 2007) is a measure of the angular momentum in the galaxy, defined via:

$$\lambda_R = \frac{< R|V| >}{R\sqrt{V^2 + \sigma^2}} \tag{1.1}$$

where $< |V| >$ indicates the mean of the absolute value of the velocity V, R the radius and

Figure 1.4: The Antennae, two colliding galaxies. Credit & Copyright: Star Shadows Remote Observatory and PROMPT/CTIO (Jack Harvey, Steve Mazlin, Rick Gilbert, and Daniel Verschatse). Image rotated by 180°.

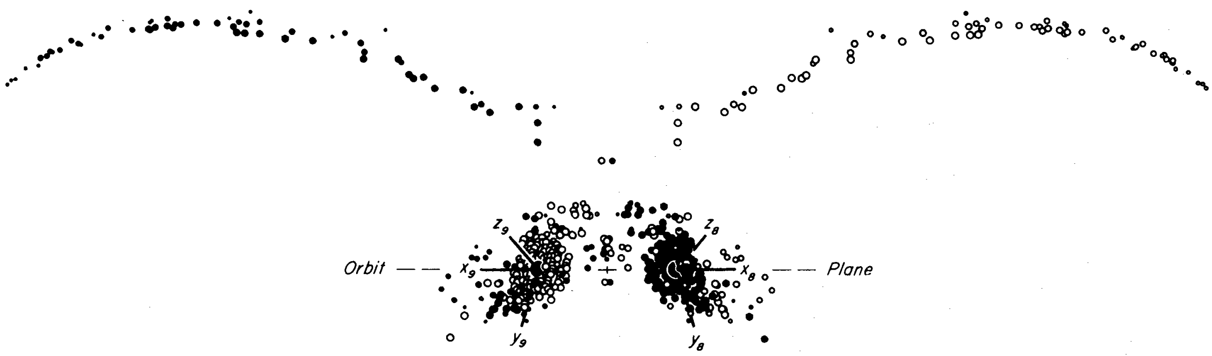

Figure 1.5: Numeric model of the Antennae galaxies, obtained from the collision of two testparticle disks. Figure taken from Toomre & Toomre (1972), Figure 23.

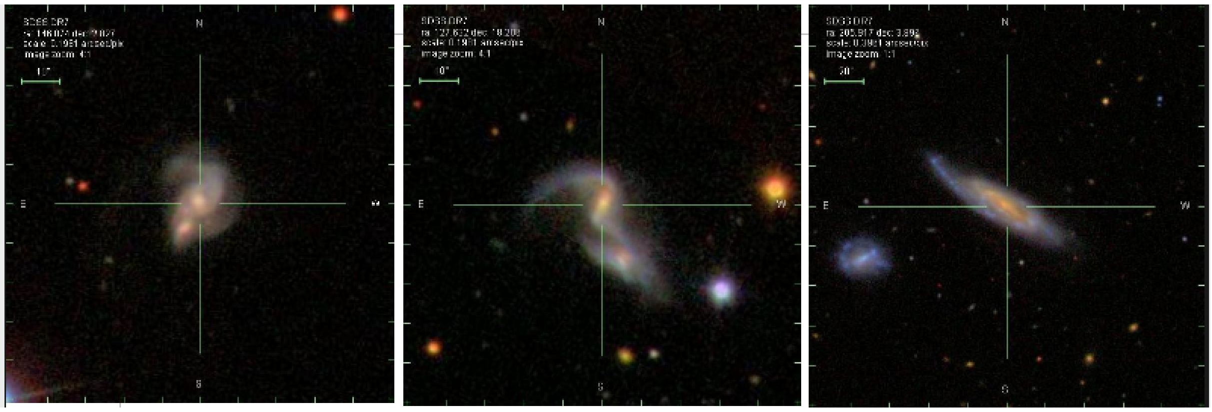

Figure 1.6: Three observed galaxy pairs representing three observed merging states, from merging (left panel) to tidal interactions (middle panel) to not disturbed (right panel). Figure taken from Lambas et al. (2012), Figure 1.

σ the velocity dispersion. λ_R can take values between 0 for a purely pressure supported system and 1 for a cold, rotating disk. Galaxies with λ_R larger (smaller) than $0.31\times\sqrt{\epsilon}$ are fast (slow) rotators measured at one effective radius (Emsellem et al., 2011).

The Atlas3D survey (Cappellari et al., 2011) investigates the complete sample of early-type galaxies in the local volume, in a cube of $1.16\cdot10^5$ Mpc^3. Figure 1.7 shows the complete Atlas^{3D} sample of 260 early-type galaxies in the ϵ-λ_R diagram. One can see that the E/S0 distinction is unphysical, as there are lot of fast rotating E galaxies and some slow rotating S0 galaxies.

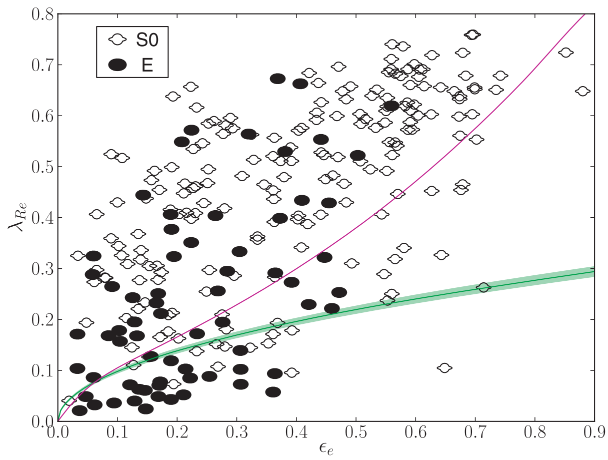

Figure 1.7: λ-ϵ diagram of the complete sample for the Atlas3D-survey. Distinction in elliptical (filled ellipses) and S0 (open symbols) galaxies, the green line marks the $\lambda = 0.31\times\sqrt{\epsilon}$ relation, the magenta line an elliptical with anisotropy $\beta = 0.65 \times \epsilon$. Figure taken from Emsellem et al. (2011), Figure 8.

A current challenge in extragalactic astronomy is to explain all types of early-type galaxies. As shown above, major mergers can in principle produce elliptical galaxies. A closer look reveals that these major mergers currently fail to reproduce slowly rotating ellipticals with low anisotropy (Burkert et al., 2008) and very round slowly rotating ellipticals (Bois et al., 2011). Other scenarios, like multiple minor mergers or mixed minor and major mergers are needed to explain the full range of elliptical galaxies from fast to slow rotating.

Observations agree with the picture that ellipticals can not only be formed by major merger interactions. Lambas et al. (2012) show that in a sample of 1959 galaxy pairs, 1082 are major and 877 are minor pairs in terms of the luminosity quotient. Imprints of the progenitor galaxy in kinematics and morphology can be found by analyzing the resulting early-type galaxy, such as shells or distinct sub populations (compare e.g. Paudel et al. 2014; Kim & Im 2013).

Looking at an observed early-type galaxy, it would be great to find a tracer hinting at the formation history, not only for information about the individual galaxy, but also as a census study to increase our knowledge about structure formation in the Universe. In this thesis, I will present the 'σ-bump', a signature in the velocity dispersion hinting at a major merger formation scenario.

This thesis is ordered as follows: In the next chapter, I will present kinematic studies in galaxies, both with direct observations and with kinematic tracers for the outskirts of galaxies, such as globular clusters and planetary nebulae. I will then show the simulation technique used in this thesis for forming the elliptical galaxies. In Chapter four, a first analysis of these objects will be given. Afterwards, I will present the σ-bump, a possible signature for major mergers, which I published as Schauer et al. (2014). A more detailed analysis for the physical reasons of the σ-bump will be given in Chapter 6. The thesis will be summarized and equipped with an outlook in the last Chapter.

2 Stellar Kinematics in Galaxies

In this chapter, I will give an overview of the kinematics of galaxies. The kinematics of galaxies are an important tool to study the properties of the individual galaxies and especially to determine their mass.

Velocities can be measured in the line-of-sight direction, as they induce a Doppler shift. Nearby galaxies can be spatially resolved, their dark matter halos can be modelled. With accumulated information from many galaxies, insight in the total mass distribution of galaxies can be obtained.

2.1 Direct Observations

In spiral galaxies, direct observations of the circular velocity were one of the first indicators for dark matter. In an exponential, rotating disk consisting of visible matter, one would expect a Keplerian decline $v_c = (GM(R)/R)^{1/2}$ as a function of radius. Observations of spiral galaxies show that the circular velocity increases and stays constant at larger radii. This can only be explained by a dark matter component, which adds a larger mass to the galaxy. Figure 2.1 shows as an example the circular velocity curve for the spiral galaxy NGC 3198. At 6 kpc, the velocity reaches its peak value and stays approximately constant afterwards, requiring not only a disk, but also a dark matter halo to explain the rotation curve (van Albada et al., 1985).

In early-type galaxies, one uses not only the first momentum of the velocity, the mean velocity, but also the second momentum, the velocity dispersion.

A general distribution, the fundamental plane, connects three basic properties of elliptical and S0 galaxies: The effective radius R_e, the average surface brightness I_e and the observed central velocity dispersion $\sigma_{||}$ (Jorgensen et al., 1996).

$$\log_{10} R_e = 1.24 \log_{10} \sigma_{||} - 0.82 \log_{10} I_e + \text{const.} \tag{2.1}$$

with a scatter of only 0.07 in $\log_{10} \sigma_{||}$ and 0.02 in $\log_{10} I_e$. The existence of this fundamental plane 'implies a strong dependence of the stellar population on the structural parameters' (Jorgensen et al., 1996, section 8). One can also determine the distance to a galaxy with its kinematic ($\sigma_{||}$) and morphology (R_e).

2.2 Tracers

The outer parts of elliptical galaxies change on very large timescales, comparably to the age of the Universe, therefore there might be fingerprints in the outskirts which could give

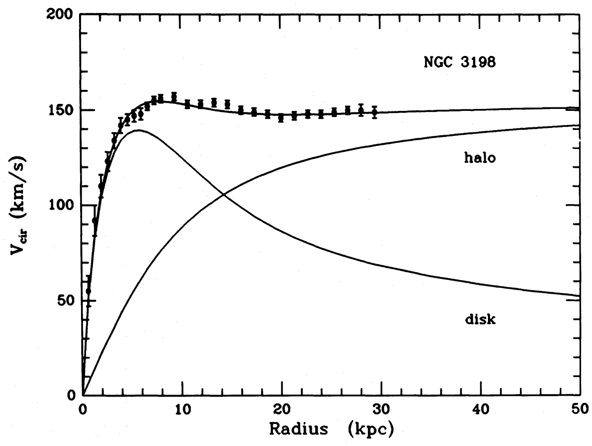

Figure 2.1: Circular velocity curve of NGC 3198, observed data points and best fit model for a disk and the dark matter halo. Figure taken from van Albada et al. (1985), Figure 4.

insight into the formation of the galaxy (Coccato et al., 2012). A huge fraction of the total mass and the total angular momentum lies outside the effective radius (90% for elliptical galaxies and 40% for spiral galaxies) (Romanowsky & Fall, 2012). Therefore, the outer parts of galaxies reveal important information.

Unfortunately, the stellar light of elliptical galaxies is very faint in the outskirts. The surface brightness of elliptical galaxies follows the empirical relation by de Vauouleurs (de Vaucouleurs, 1953)

$$\Sigma(r) = \Sigma_e \exp -7.67[(r/R_{\text{eff}}])^{1/4} - 1] \tag{2.2}$$

which drops off very fast. In addition it is not possible to study the kinematics of the outer stellar halo using gas, beacause elliptical galaxies are very gas poor (Coccato et al., 2012).

The disks of spiral galaxies can be well observed out to large radii. Other stellar components in late-type galaxies like a thick disk or a stellar halo are very faint and therefore difficult to observe as well.

If the stellar light is too faint to be observed directly, tracers are needed. Two examples are planetary nebulae and globular clusters, which will be presented in the two consecutive subsections.

2.2.1 Planetary Nebulae

A possible tracer for the kinematics of galaxies are planetary nebulae. Planetary nebulae are stars in a late evolutionary state, namely white dwarfs which have blown away their outer shells. They are well observable, as they emit up to 15% of their light in the OIII emission line at $\lambda = 5007\,\text{Å}$ (Dopita et al., 1992). Therefore, planetary nebulae can be detected as single objects in galaxies at a distance of several Mpc. Instruments like the planetary nebulae spectrograph (PNS) exist (Douglas et al., 2002) to measure the kinematics in early-type galaxies. With the PNS, position and radial velocity can be obtained with one image.

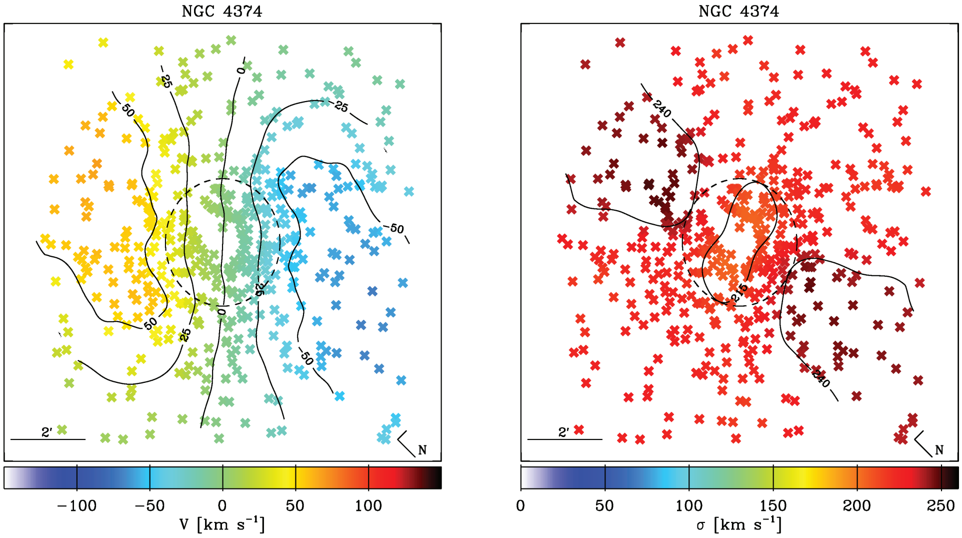

Figure 2.2: Distribution of planetary nebulae in NGC 4373. The smoothed velocity (left panel) and velocity dispersion (right panel) maps are shown with color coding. The dashed ellipse marks $2R_{\mathrm{eff}}$. Figure taken from (Coccato et al., 2009), Figure 3, forth row.

An example of the use of the PNS is shown in Figure 2.2 for galaxy NGC 4374. The distribution of planetary nebulae in galaxy is displayed as well as their velocity and velocity dispersion, indicated by a color bar. Similar studies for planetary nebulae exist e.g by Méndez et al. (2001, 2008, 2009); Napolitano et al. (2009, 2011); Romanowsky et al. (2003).

Not only early-type galaxies can be studied with planetary nebulae, spiral galaxies reveal interesting structures as well. E.g. Merrett et al. (2006) study over 2600 PNe in the Andromeda Galaxy and are even able to resolve satellite galaxies. Shih & Méndez (2010) study planetary nebulae in NGC 891, and reveal rotation patterns above and below the galactic plane.

2.2.2 Globular Clusters

Another possibility to trace the kinematics of elliptical galaxies at large radii or to investigate stellar halos are globular clusters. In some galaxies, there exists a color bimodality, distinguishing globular clusters in a metal rich (red) and a metal poor (blue) subpopulation. It is suggested that red globular clusters trace the kinematics of the stellar population and blue globular clusters may have accreted later (Schuberth et al., 2010; Pota et al., 2013). Figure 2.3 displays stellar data as well as the two sub populations of globular clusters in NGC 2768. This is a very nice example which shows that in this galaxy, red globular clusters trace the stellar population.

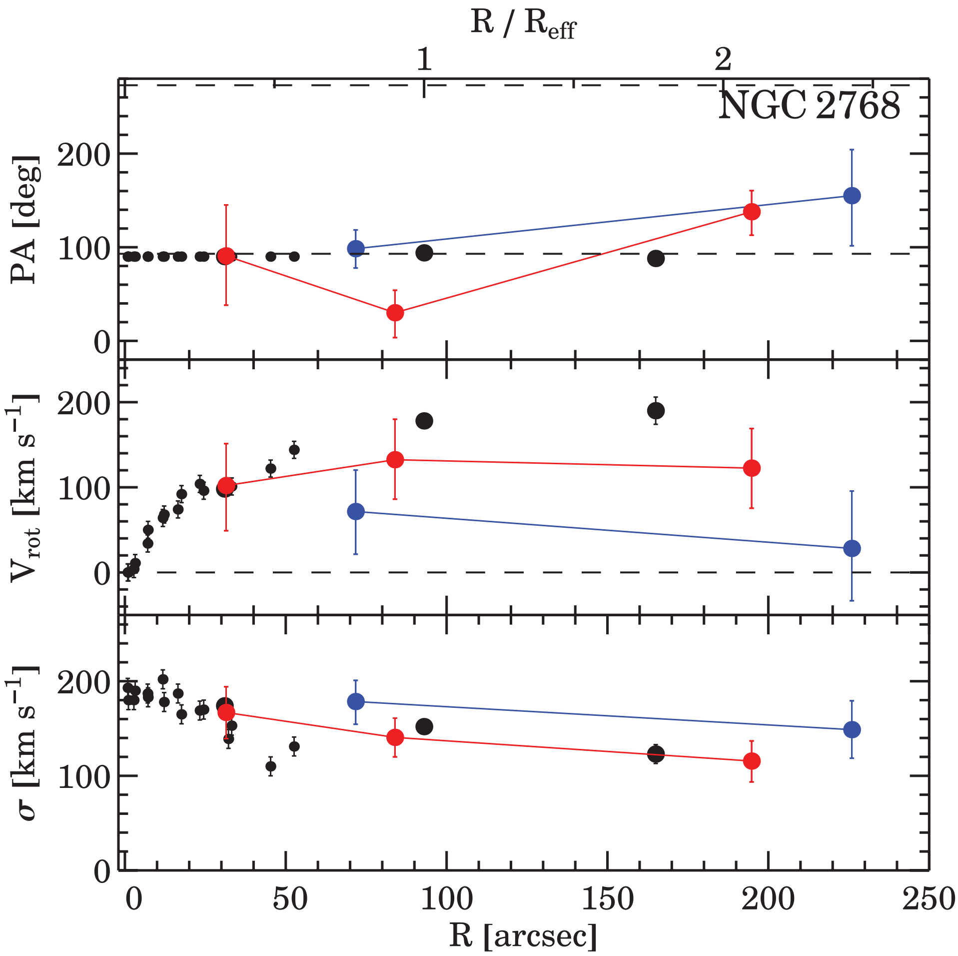

Figure 2.3: Globular clusters of NGC 2768. Kinematic position angle (top panel), rotational velocity (middle panel) and velocity dispersion (bottom panel) are shown for the red (red points) and blue (blue points) globular cluster subpopulations and additional stellar data (black points) from Fried & Illingworth (1994). Figure taken from Pota et al. (2013), Figure 11.

Similar studies on the kinematics of early-type galaxies have been performed, e.g. by Foster et al. (2011); Strader et al. (2011). The sample sizes vary from few tens of globular clusters to several hundreds (compare Pota et al. 2013). Some of these data are publicly available and are used in Schauer et al. (2014), which is part of this thesis.

3 Setup of the Simulations

In this chapter, I will describe the sets of simulations I use for my analysis. To study the kinematics of galaxies, simulations need to be sufficiently large in both size and resolution, especially for slow rotating ellipticals (Bois et al., 2010). A first possibility is given by studying isolated galaxies. My first sample of elliptical galaxies is made of major mergers, namely two isolated galaxies colliding with each other on a parabolic orbit. With this technique, one can focus on the intrinsic properties of the galaxies and can be sure not to be dominated by other features. The calculation in an isolated environment without the potential of a central galaxy cluster or infall and disturbance by satellite galaxies or gasous streams leads to an artificial, somehow unphysical setup. One big advantage is that all simulated particles can be used for the analysis, unlike in other simulations, where the region of interest is cut out of a larger volume.

The second simulation technique is by resimulated or zoomed-in galaxies. Here, a full cosmological simulation with comparably low resolution has been performed. At z=0, regions which might host galaxies are cut out and simulated again with a higher resolution at high redshift, keeping the environment physical but increasing the resolution.

All simulated galaxies which I will analyse in the course of this work are performed by N-body simulations. In the next subsection, I describe the major merger simulation setup for two samples used in this Master thesis. Subsequently, I will describe the cosmological simulation used for a comparison study in this thesis.

3.1 Major Mergers

In total, we have two sets of elliptical galaxies formed by major mergers, one produced by Peter Johansson (compare Johansson et al. (2009a) and Johansson et al. (2009b)) which we will call sample P from now on, the other one by the author herself, called sample A.

3.1.1 The Progenitor Galaxies

For setting up a merger, we first need to create the progenitor spiral galaxies. The progenitor galaxies from both sample P and sample A are constructed in a way described by Johansson et al. (2009a) and Johansson et al. (2009b).

The mass of the halo M_{vir} can be defined via the virial velocity v_{vir} where v_{vir} corresponds to an overdensity of $\Delta_{\mathrm{vir}} = 200$:

$$M_{vir} = \frac{v_{vir}^3}{10GH_0}. \tag{3.1}$$

The virial velocity v_{vir} is related to the virial radius R_{vir}

$$R_{vir} = \frac{v_{vir}}{10H_0}. \tag{3.2}$$

The Hubble parameter of $H_0 = 71\,\mathrm{km\,s^{-1}\,Mpc^{-1}}$ is chosen according to the WMAP1 results by combining the WMAP1 measurements with other available data from that time (Spergel et al., 2003). It sometimes is expressed as $h = 0.71$, such that $H_0 = 100 \times h\,\mathrm{km\,s^{-1}\,Mpc^{-1}}$. Except for merger 31 OBH 09 320 in sample P, the virial velocity is set to $v_{vir} = 160\,\mathrm{km\,s^{-1}}$, corresponding to $M_{vir} = 9.53{\cdot}10^{11}\,h^{-1}\,M_\odot$, a Milky Way like mass. The exceptional merger 31 OBH 09 320 has a virial velocity $v_{vir} = 320\,\mathrm{km\,s^{-1}}$ and therefore the eight times higher mass $M_{vir} = 7.62{\cdot}10^{12}\,h^{-1}\,M_\odot$. There a different sizes of the progenitors: major progenitors with a mass described above, minor progenitors and mini progenitors. Major progenitors are used for 1:1 mergers. Minor progenitors include 1/3, mini progenitors 1/10 of the mass of a major progenitor.

The galaxy is build up by the following components according to Springel et al. (2005):

1. A **dark matter halo** with a concentration parameter $c = R_{vir}/r_s = 9$ according to the NFW-halo model (Navarro et al., 1997)

$$\rho_{dm,\mathrm{NFW}}(r) = \frac{\rho_0}{\frac{r}{r_s}(1+\frac{r}{r_s})^2}. \tag{3.3}$$

   The halo itself is build by a Hernquist-model by (Hernquist, 1990)

$$\rho_{dm,\mathrm{Hernquist}}(r) = \frac{M_{dm}}{2\pi}\frac{a}{r(r+a)^3}. \tag{3.4}$$

   The Hernquist profile is chosen as a fast drop-of in the outer parts is wanted to study isolated halos. In the inner part, the Hernquist and the NFW halo behave similarly, therefore this choice seems reasonable in terms of balancing the physical properties and the numerical requirements. The scale parameters a for the Hernquist-profile and c for the NFW-profile are related by setting the virial mass M_{vir} constant and therefore

$$a = r_s\sqrt{2[\ln(1+c) - c/(1+c)]} = r_s\sqrt{2[\ln(1+9) - 9/(1+9)]} \approx 1.67 r_s \tag{3.5}$$

2. A **baryonic disk** containing a mass fraction $m_d = 0.041$ of the total virial mass, $M_d = m_d M_{vir}$. The disk follows a simple exponential law with a disk scale length r_d, constructed after Mo et al. (1998). Thereby it is assumed that the specific angular momentum is conserved. Therefore, fraction of the disk angular momentum, j_d, is assumed to be equal the fraction of the disk mass m_d. In addition, the halo spin $\lambda = 0.033$ is constant for all models. The disk scale length is calculated by

$$r_d = \frac{1}{\sqrt{2}}\frac{j_d}{m_d}\lambda R_{vir} f_c^{-1/2} f_r(\lambda, c, j_d, m_d). \tag{3.6}$$

f_c and f_r are dimensionless parameters, f_c corresponds to a deviation from a NFW-halo to an isothermal sphere and can be approximated as $f_c \approx 2/3 + (c/21.5)^{0.7}$. f_r is an integral over the rotation curve and a measure for the NFW-halo as well as for gravitational effects of the disk. With $\lambda' = (j_d/m_d)\lambda$, a good approximation of f_r is $f_r \approx (\lambda'/0.1)^{-0.06+2.71m_d+0.0047/\lambda'}(1 - 3m_d + 5.2m_d^2)(1 - 0.019c + 0.00025c^2 + 0.52/c)$.

For the major progenitor galaxies, $r_{d,1} = 3.5\,\mathrm{kpc}$ and for the minor progenitors, $r_{d,2} = 2.4\,\mathrm{kpc}$. The vertical scale length $z_0 = 0.2r_d$ is set constant.

3. Part of the baryonic disk is made of **gas**, the rest of the baryonic mass are stars. For different simulations in sample P, the gas fraction, f_{gas}, varies from 0% to 80%. The simulations of sample A all have a gas fraction of $f_{gas} = 20\%$.

4. A **stellar bulge** with a mass fraction $m_b = 0.01367 = m_d/3$ is created following a profile from Hernquist (1990). Its bulge scale length is treated like the vertical scale length, it is also set to $b = 0.2r_d$. Some of the galaxies in sample P do not contain a bulge.

5. In the center of the galaxy, a **black hole** (BH) is included as a sink particle. Its mass is set to $1 \cdot 10^5\,M_\odot$ for a all simulations except simulation 'ASF' with $1.59 \cdot 10^7\,M_\odot$, which follows the black hole mass – velocity dispersion relation from Tremaine et al. (2002):

$$\log(M_{\mathrm{BH}}/M_\odot) = \alpha + \beta \cdot \log(\sigma/\sigma_0) \tag{3.7}$$

with reference $\sigma_0 = 200\,\mathrm{km\,s^{-1}}$. Tremaine et al. (2002) measured values of $\beta = 4.02 \pm 0.32$ and $\alpha = 8.13 \pm 0.06$. Regarding the nomenclature of Johansson et al. (2009a), the simulations described here with 'O' in their name correspond to the 'B2' simulations, the simulation with 'A' in its name here corresponds to the 'O2' simulation.

The progenitor galaxy is shown from three major directions in Figure 3.1. Different colors indicate different components: dark matter is shown in black, the stellar part of the disk in blue, the gaseous part in green and the bulge in red. One recognizes a disk galaxy without a spiral structure.

In addition, I show in Figure 3.2, the density profiles for the different components of the same progenitor galaxy. The color scheme is the same like in Figure 3.1. One can see that in the inner radii, the density is dominated by the stellar components, at larger radii, by the dark matter component.

The mass resolution for baryonic particles is $M_{\mathrm{gas}} = M_{\mathrm{stars}} = 1.30 \cdot 10^5\,h^{-1}\,M_\odot$. For dark matter particles, $M_{\mathrm{DM}} = 2.25 \cdot 10^6\,h^{-1}\,M_\odot$. For the one galaxy with initial virial velocity $320\,\mathrm{km\,s^{-1}}$, the galaxy is less resolved, with $M_{\mathrm{gas,320}} = M_{\mathrm{stars,320}} = 1.04 \cdot 10^6\,h^{-1}\,M_\odot$ and $M_{\mathrm{DM,320}} = 1.80 \cdot 10^7\,h^{-1}\,M_\odot$. The number of particles is listed in Table 3.1. For the major progenitors, each galaxy hosts in total 800 000 particles, for the minor progenitors, 800000/3.

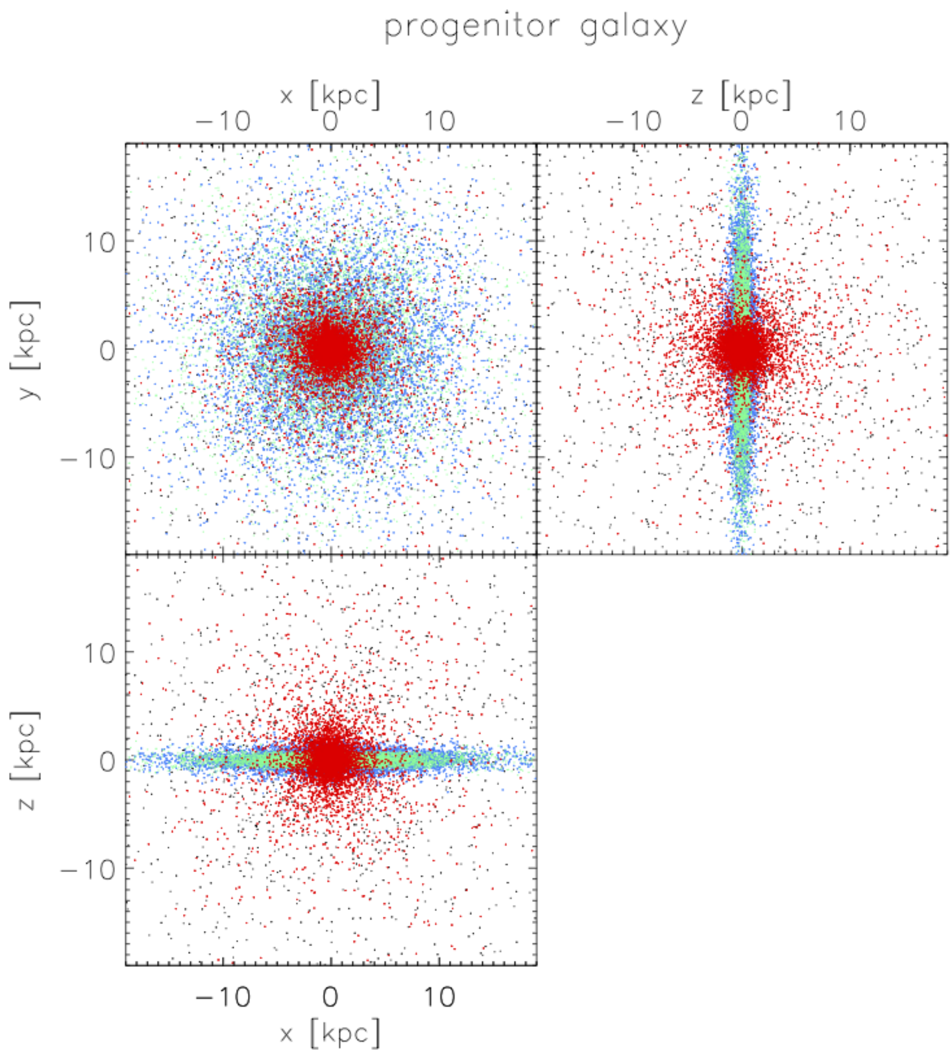

Figure 3.1: Appearance of a major progenitor galaxy in three projections. The components are plotted in different colors: dark matter (black), stellar disk (blue), gaseous disk (green) and bulge (red). For a better view, every 8th particle is shown in this figure.

3.1.2 Merger Setup

As in Johansson et al. (2009b), we denote the primary galaxy with 'p' and the secondary galaxy with 's'. The progenitor galaxies are set on parabolic orbits according to Naab & Burkert (2003). They are initially separated by $R_{\rm init} = 0.5(R_{{\rm vir},p} + R_{{\rm vir},s})$. The orbits are

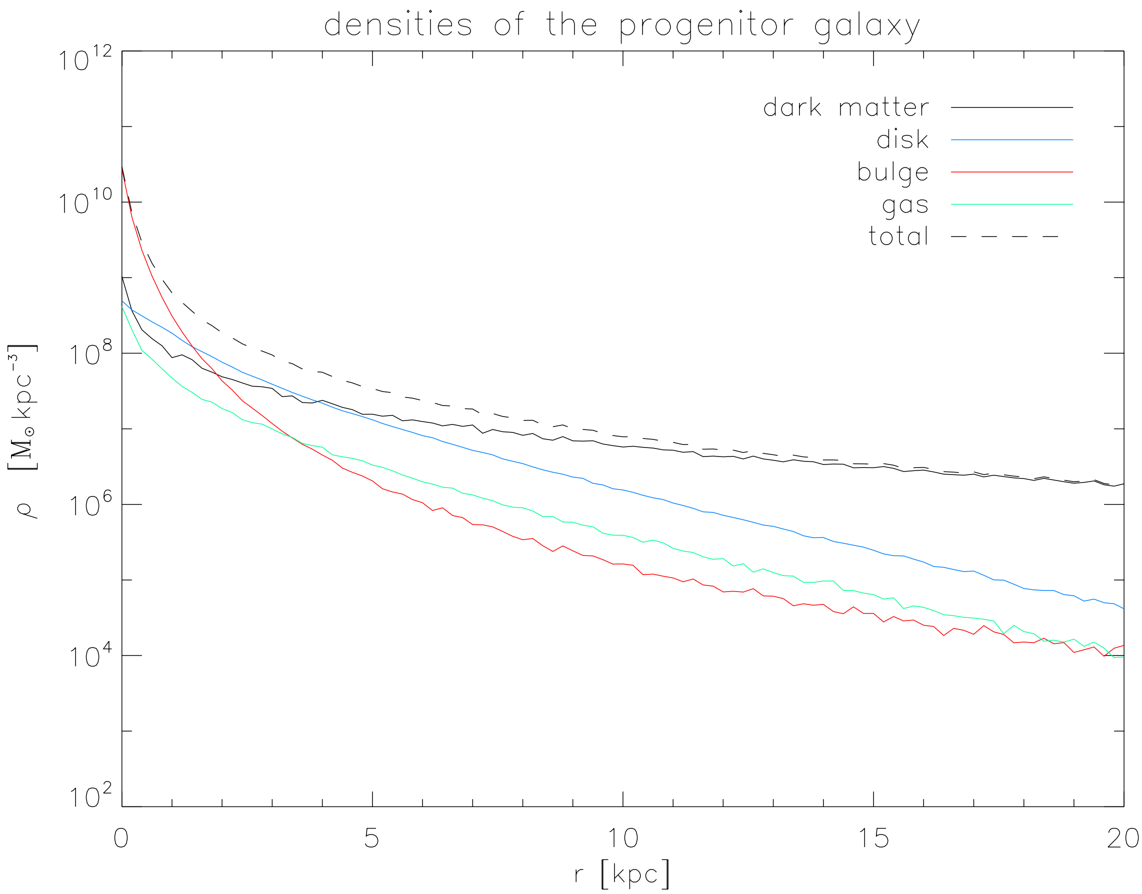

Figure 3.2: Density profile of a major progenitor galaxy for all components of the galaxy. For the color scheme see Figure 3.1.

constructed in a way that the pericentric distance equals $r_{\text{peri}} = r_{d,p} + r_{d,s}$.

In both samples, we study major merger collisions, in addition to two minor merger collisions in sample A. In sample P, for five simulations, the mass ratios of the progenitor galaxies are 1:1 (major progenitor merging with major progenitor), for four simulations, they are 3:1 (major progenitor merging with minor progenitor), and the last simulation is a remerger of a 3:1 simulation with a major progenitor (elliptical progenitor merging with major progenitor). In sample A, there are four 1:1 mergers (major progenitor merging with major progenitor), three 3:1 mergers (major progenitor merging with minor progenitor) and two 10:1 minor mergers (major progenitor merging with mini progenitor).

We choose different orbital parameters, varying the inclination angles i_1 and i_2 of the progenitors with respect to the orbit plane and the pericenter arguments ω_1 and ω_2, i.e. the angles with respect to the pericenter. Figure 3.3 schematically shows these two angles. For i_1, i_2, ω_1 and ω_2, we choose orbits from Naab & Burkert (2003) for sample P and in

Progenitor	N_{gas}	N_{disk}	N_{bulge}	N_{DM}
major progenitor	60 000	240 000	100 000	400 000
minor progenitor	20 000	80 000	33 333	133 333
elliptical progenitor	80 000	320 000	133 333	533 333

Table 3.1: Particle numbers of the progenitor galaxies.

addition extreme orbits for sample A. In table 3.2, the orbit geometries are listed.

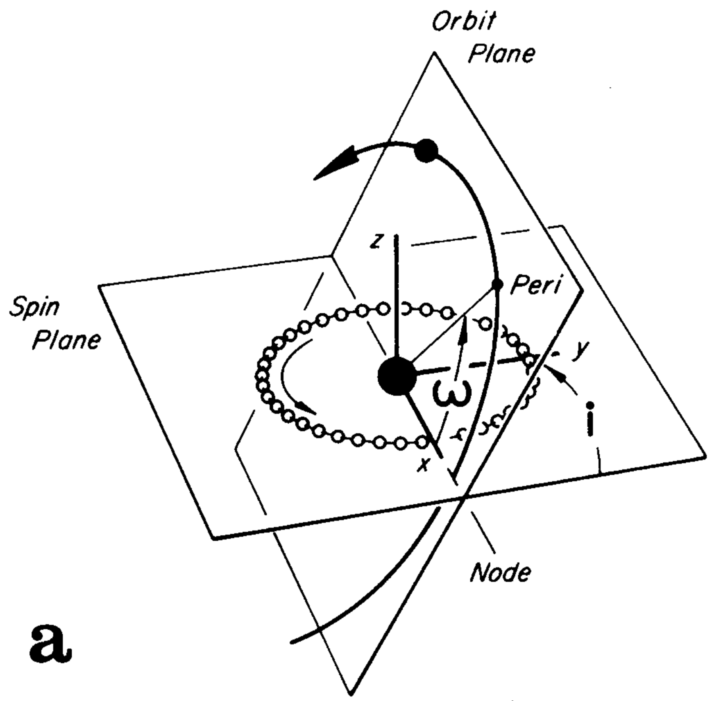

Figure 3.3: Orbital geometry: Sketch of inclination angle and pericenter argument. Figure taken from Toomre & Toomre (1972), Figure 6 (a).

In all but two cases, the simulations in sample P and the minor mergers in sample A are run for 3 Gyrs. The simulations 11 OBH 13 and 31 OBH 13 in sample P are run for 10 Gyrs and all major mergers in sample A are run for 6 Gyrs. The galaxies first encounter after 0.5 Gyrs and are finally merged at about 1.5 Gyrs. A snapshot of the simulation is taken every 20 Myrs, so that for the 3 Gyrs simulation, we have 150 snapshots. Tables 3.3 and 3.4 show the initial properties of samples A and P, respectively.

Figure 3.4 shows some snapshots of the 3:1 merger in sample A on an A02 orbit, where the progenitors have a 90° inclination angle to each other. Stars of the disk are shown in red, stars of the bulge in green and stars which formed during the simulation in blue. Other colors indicate that there are more than one type of stars, e.g. yellow is a mixture

Orbit name	i_1	i_2	ω_1	ω_2
G01	0	0	180	0
G09	-109	0	180	0
G13	-109	60	180	0
A01	-109	-60	0	0
A02	90	0	180	0
A03	0	0	0	0
A04	-90	0	180	0

Table 3.2: Orbit geometries: inclination angles and pericenter arguments. The first three orbits are from Naab & Burkert (2003).

Model	Ratio$^{(a)}$	Orbit$^{(b)}$	$f_{\mathrm{gas}}^{(c)}$	bulge$^{(d)}$	BH$^{(e)}$	$v_{\mathrm{vir}}^{(f)}$	t
11 NB NG 13	1:1	G13	0.0	no	yes	160	3
11 NB OBH 13	1:1	G13	0.2	no	yes	160	3
11 NG 13	1:1	G13	0.0	yes	yes	160	3
11 OBH 09	1:1	G09	0.2	yes	yes	160	3
11 OBH 13	1:1	G13	0.2	yes	yes	160	10
31 ASF 01	3:1	G01	0.2	yes	no	160	3
31 O8BH 13	3:1	G13	0.8	yes	yes	160	3
31 OBH 09 320	3:1	G09	0.2	yes	yes	320	3
31 OBH 13	3:1	G13	0.2	yes	yes	160	10
mix 11 OBH 13	1:1	G13	0.2	yes	yes	160	3

Table 3.3: Binary merger simulation sample P, (a) initial mass ratio of the two galaxies; (b) Orbit type according to Naab & Burkert (2003); (c) Initial gas fraction of the disks of the progenitor galaxies; (d) Do the progenitor galaxies contain a bulge? (e) Do the progenitor galaxies contain black holes? (f) Initial virial velocity in $\mathrm{km\,s^{-1}}$; (g) Total duration of the simulation in Gyrs; compare Table 1 of Schauer et al. (2014).

Model	Ratio$^{(a)}$	Orbit$^{(b)}$	$f_{\rm gas}^{(c)}$	bulge$^{(d)}$	BH$^{(e)}$	$v_{\rm vir}^{(f)}$	$t^{(g)}$
11 OBH 01 20 160	1:1	G01	0.2	yes	yes	160	6
11 OBH A02 20 160	1:1	A02	0.2	yes	yes	160	6
11 OBH A03 20 160	1:1	A03	0.2	yes	yes	160	6
11 OBH A04 20 160	1:1	A04	0.2	yes	yes	160	6
31 OBH 01 20 160	3:1	G01	0.2	yes	yes	160	6
31 OBH 13 20 160	3:1	G13	0.2	yes	yes	160	6
31 OBH A02 20 160	3:1	A02	0.2	yes	yes	160	6
101 OBH 13 20 160	10:1	G13	0.2	yes	yes	160	3
101 OBH 09 20 160	10:1	G09	0.2	yes	yes	160	3

Table 3.4: Binary merger simulation sample A, (a) initial mass ratio of the two galaxies; (b) Orbit type according to Naab & Burkert (2003) and Table 3.2; (c) Initial gas fraction of the disks of the progenitor galaxies; (d) Do the progenitor galaxies contain a bulge? (e) Do the progenitor galaxies contain black holes? (f) Initial virial velocity in $\mathrm{km\,s^{-1}}$; (g) Total duration of the simulation in Gyrs;

of red and green and therefore indicates that disk and bulge stars are present or white is a mixture of red, green and blue and therefore stars of all kinds can be seen.

The field of view for Figure 3.4 is chosen to be $120\,\mathrm{kpc} \times 120\,\mathrm{kpc}$. The first panel (snapshot 14) shows the two progenitor galaxies before the collision. The second panel (snapshot 24) displays the first bypass of the galaxies, which already disrupts the structure of the progenitors. The effect on the disks of the progenitors can be best seen in panel three (snapshot 32), where the disk gets disrupted and previously discussed tidal features show up. The next panel (snapshot 58) shows the two progenitors shortly before their second encounter. New tails have formed, gravity is about to mix the two galaxies together. Panel five (snapshot 70) shows the galaxies after the second encounter, where the internal structure gets destroyed. One galaxy is formed out of two, while the outer parts are violently disturbed and partly ejected. The inner parts start to relax in panel six (snapshot 87). A shell is moving outwards, best seen in the upper right and lower left of the panel. In the next panel (snapshot 104), one can see that the outer parts are still not relaxed. Most of the simulations run for 3 Gyrs, therefore I show in panel seven the fully formed elliptical after 3 Gyrs (snapshot 149). Except for the outer parts and some movement and rotation, which are unfortunately present in the simulation setup, panel eight shows the same elliptical after 6 Gyrs (snapshot 299), the end of this simulation.

3.1.3 Further Properties of the Simulation Setup

Other physical parameters are included in the simulation, which do not have a substantial effect on the kinematics in the outer regions. For completeness, I list them in this section.

- Star formation and supernova feedback are included as described in Springel & Hernquist (2003), where the interstellar medium 'is treated as a two-phase medium (Mc-

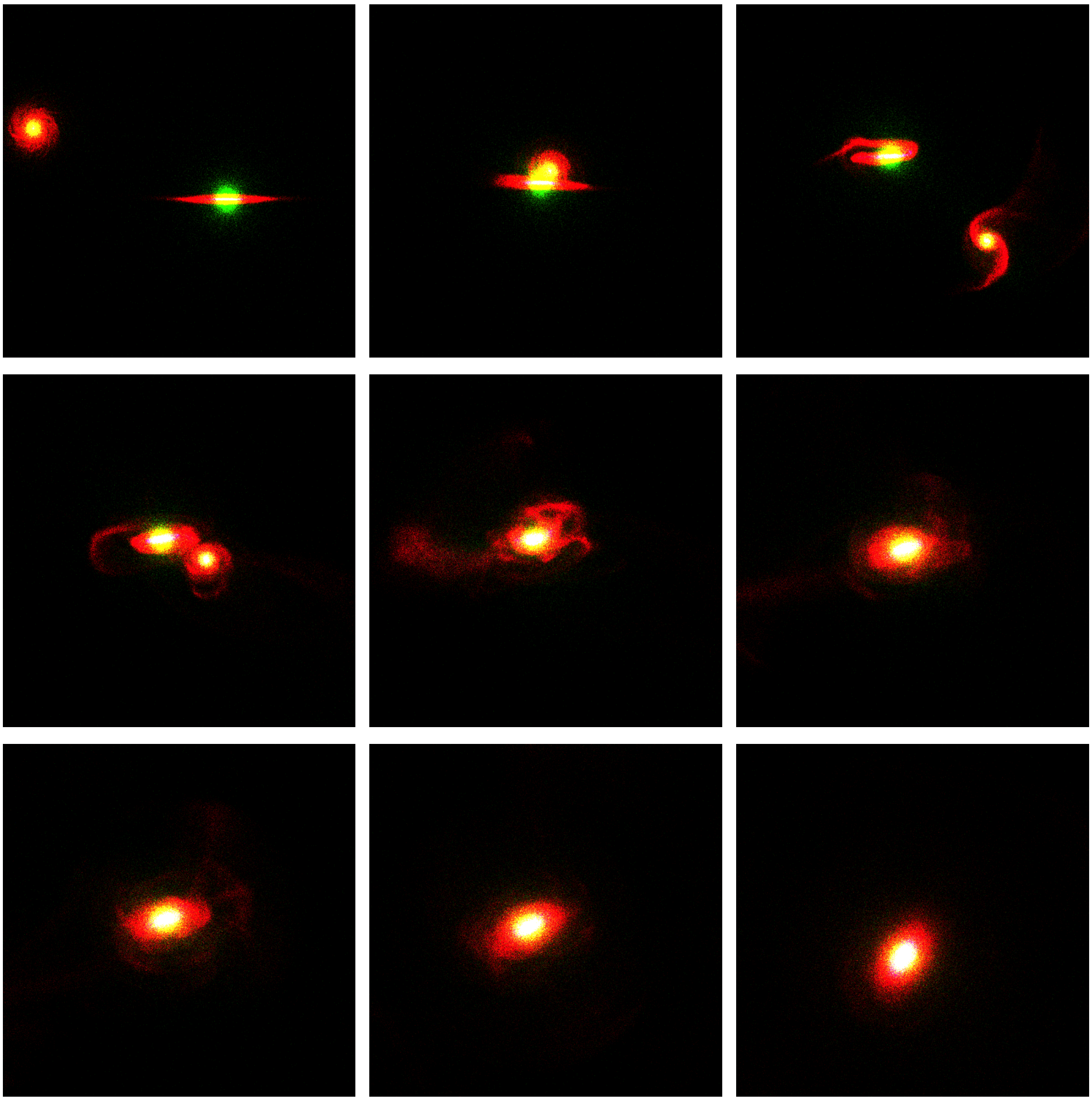

Figure 3.4: Snapshots of a 3:1 simulation on a 90° inclined orbit. Panels run from left to right and from top to bottom, showing the timesteps after 300, 500, 660, 1180, 1420, 1760, 2100, 3000 and 6000 Myrs (snapshots 14, 24, 32, 58, 70, 87, 104, 149 and 299).

Kee & Ostriker, 1977; Johansson & Efstathiou, 2006) in which cold clouds are embedded in a tenuous hot gas at pressure equilibrium' (Johansson et al., 2009a).

- Black hole merging is kept efficient. If the black holes are within the smoothing length of each other and their velocities are below the local sound speed, they merge instantaneously (Johansson et al., 2009a).

- The black hole accretion follows the Bondi-Hoyle-Lyttleton parametrization
$$\dot{M}_B = \frac{4\pi\alpha G^2 M_{\mathrm{BH}}^2 \rho}{(c_s^2 + v^2)^{3/2}} \tag{3.8}$$
where the efficiency parameter α is set to 25 (compare Johansson et al. (2009b)). The accretion depends on the density ρ, the sound speed c_s of the surrounding gas and the black hole velocity v.

- The gravitational softening lengths for baryonic particles and the black holes are set to $\epsilon_{\mathrm{stars}} = \epsilon_{\mathrm{gas}} = \epsilon_{\mathrm{BH}} = 0.02 h^{-1}$kpc and to $\epsilon_{\mathrm{DM}} = 0.083\, h^{-1}$ kpc for dark matter particles.

All simulations of sample P are performed using the GADGET-2 code from Springel (2005). It is a N–body gravity and smoothed particle hydrodynamics code on a tree structure. For the simulations in sample A, its successor GADGET-3 is used.

3.2 Cosmological Resimulated Galaxies

The second method used in this thesis to construct elliptical galaxies are cosmological zoom galaxies. These are resimulations of halos in a dark matter simulation. The sample presented in this section was published by Oser et al. (2010) and also used by Remus et al. (2013).

3.2.1 The Cosmological Simulation

The 'parent' simulation is a dark matter only cosmological simulation in a cubic box with a comoving side length of $72\, h^{-1}$ Mpc. It hosts $512^3 \cdot 10^8$ particles with a mass of $M_{\mathrm{DM}} = 2 \cdot 10^8\, h^{-1}\, M_\odot$ each. The WMAP–3 parameters (Spergel et al., 2007) are used for the cosmological setup: the Hubble parameter $h = 0.72$, the baryonic and dark matter mass fractions $\Omega_m = 0.26$ and $\Omega_\Lambda = 0.74$, $\sigma_8 = 0.77$ and the power spectrum's initial slope $n_s = 0.95$. The comoving gravitational softening length is set to the constant value $2.52\, h^{-1}$ kpc.

The simulation starts at redshift $z \sim 43$ and evolves to $z = 0$ with the initial conditions from GRAFICI and LINGERS (Bertschinger, 1995). A total of 95 snapshots is created, separated by $\Delta a = 0.01$. The first snapshot is taken at $a = 0.06$, the last at $a = 1$.

3.2.2 Resimulation Technique

At $z = 0$, halos are found in the parent dark matter simulation with a friend-of-friend algorithm and their centers are located via a shrinking sphere method (compare Power et al. 2003). All dark matter particles within a radius of $2R_{vir}$ (defined as in the major merger simulation) of the halo center at any snapshot are followed back in time to the first snapshot. There, they are replaced by higher resolved gas and dark matter particles with $\Omega_{\rm gas} = \Omega_{\rm stars} = 0.044$ and $\Omega_{\rm DM} = 0.216$. This is 'an efficient mechanism to reduce contamination with massive boundary particles' (Oser et al., 2010, section 2.2).

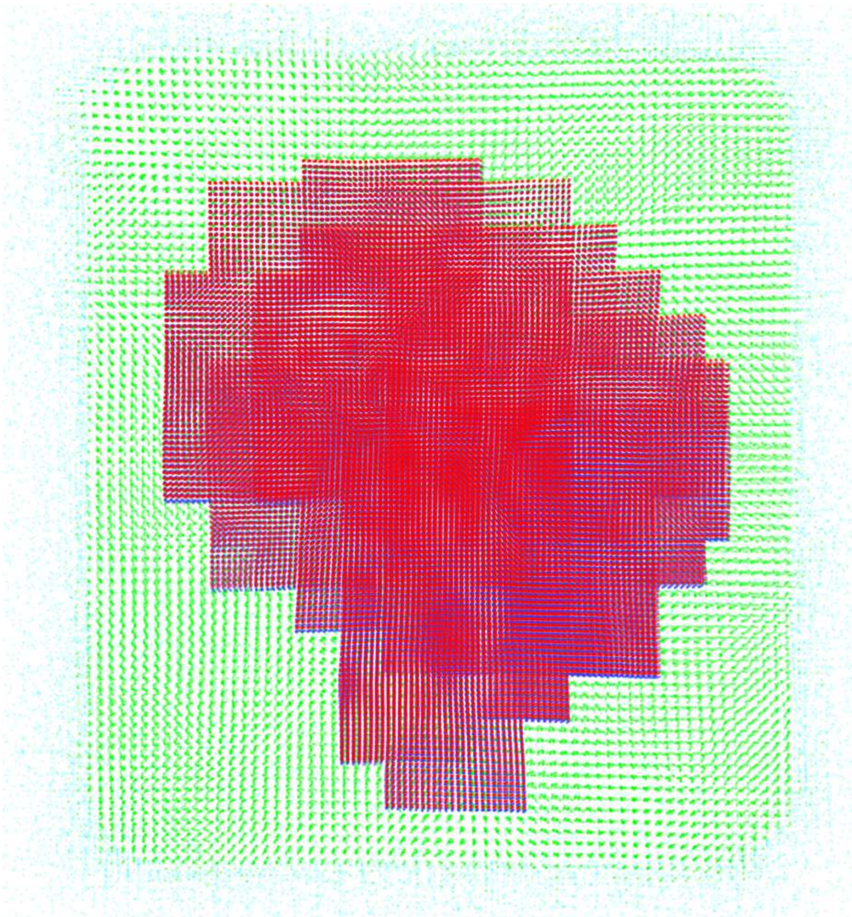

Figure 3.5: Halo 0408 at the first snapshot, filled up with gas (red) and dark matter (blue) particles in high resolution and original dark matter particles (green) in low resolution. Figure taken from Oser et al. (2010), Figure 3.

Figure 3.5 shows one of the halos of Oser et al. (2010)'s simulation traced back to the starting point at $z \sim 43$. The resolution is then increased by a factor of two in every direction, corresponding to eight times the mass resolution. To this end, every dark matter particle of mass $2 \cdot 10^8\,h^{-1}\,M_\odot$ is replaced by eight dark matter particles of mass $M_{\rm DM} = 2.1 \cdot 10^7\,h^{-1}\,M_\odot$ (blue) and eight gas particles of mass $M_{\rm gas} = 4.2 \cdot 10^6\,h^{-1}\,M_\odot$ (red). In the course of the simulation, star particles with the same mass form out of some of the gas particles. To account for gravitational effects from the surrounding features, a safety region of $1\,h^{-1}\,$Mpc (green) is installed around the high resolution region and particles further away are merged with increasing mass. The softening lengths for the new particles are decreased to $\epsilon_{\rm DM} = 890\,h^{-1}\,$pc for the highly resolved dark matter particles and to $\epsilon_{\rm stars,gas} = 400\,h^{-1}\,$pc for the baryonic matter.

For smaller halos, resimulations with higher resolution are run as well. In the '4x' simulation, the spacial resolution is doubled again. In the '8x' simulation, the spacial resolution is doubled with respect to the '4x' simulation. Some of the halos are counted twice as they have been resimulated with different resolutions. In total, 15 halos are resimulated with 'normal 2x' high resolution, 14 halos with '4x' resolution and one halo with '8x' resolution. The names, resolutions and the number of particles from the resimulations associated with the halos are listed in Table 3.5.

3.2.3 Further Properties of the Simulation Setup

Several physical and numerical properties of the simulation can be found in Oser et al. (2010). The code used is again the GADGET-2 code (Springel, 2005). The star formation and feedback is treated in the same way as in the major merger simulations (compare section 3.1).

Halo name	Resolution	N_{gas}	N_{stars}	N_{dm}
M0004	2x	2 142 925	1 334 456	3 567 556
M0040	2x	579 930	440 626	1 076 354
M0053	2x	331 005	275 805	680 658
M0069	2x	354 378	306 742	717 207
M0089	2x	214 528	182 465	429 880
M0094	2x	210 596	164 402	405 392
M0125	2x	200 865	146 889	369 078
M0162	2x	134 454	106 554	253 307
M0163	2x	139 297	119 486	277 721
M0175	2x	127 745	117 170	285 358
M0189	2x	136 060	117 763	266 984
M0190	2x	103 075	98 844	203 975
M0204	2x	102 722	99 548	216 731
M0204	4x	603 631	777 397	1 512 450
M0209	2x	118 459	97 601	241 518
M0215	2x	100 251	87 072	204 062
M0227	4x	711 665	868 103	1 606 982
M0408	4x	335 836	386 642	745 517
M0501	4x	263 577	368 654	721 885
M0616	4x	209 311	342 380	585 698
M0664	4x	189 308	286 648	561 902
M0858	4x	59 962	129 730	305 801
M0959	4x	162 463	207 309	413 629
M0977	4x	70 772	98 295	163 174
M1196	4x	105 537	156 942	287 199
M1646	4x	80 585	128 528	223 547
M2283	4x	39 768	77 710	109 101
M4323	4x	28 262	60 717	80 315
M6782	4x	22 323	49 171	46 862
M6782	8x	53 675	187 280	206 982

Table 3.5: Basic properties of the resimulated galaxies: Halo name, resolution factor and total number of particles in the extracted resimulated halo. Compare also Oser et al. (2010), Table 1.

4 Basic Properties of the Resulting Ellipticals

In this chapter, I will present the resulting ellipticals and give a first overview of them. Basic properties like the resulting virial radius, the effective radius, the morphology and the density will be presented.

4.1 Ellipticals from Major Mergers

For the letter Schauer et al. (2014), one example galaxy, namely '11 OBH 13', has been chosen. Therefore, I will present some properties mainly for galaxy 11 OBH 13.

At first, the resulting elliptical galaxy needs to be centered in the reference frame. This is done by calculating the center of mass $\mathbf{r}_0$ for all stellar particles. A first inspection by eye gives an estimate of the position of the galaxy within a cube with side length 20 kpc. The center of mass is calculated by:

$$\mathbf{r}_0 = \frac{1}{M} \sum_{i=1}^{N} m_i \mathbf{r}_i \tag{4.1}$$

with N the number of particles in the cube, M the total stellar mass in the cube and m_i and $\mathbf{r}_i$ the masses and positions of the particles in the cube. After that, all particles are recentered with respect to the center of mass. To increase the precision, this process is repeated iteratively. Therefore, the side lengths of the cube are iteratively shrunk by 20%, the new center of mass is calculated and the galaxy is recentered with respect to the new origin. This runs until the number of particles in the final cube leads to a Poisson error of 1%: $1/\sqrt{N} < 1\%$ or equivalently $N > 10000$.

In a next step, the resulting galaxy is oriented. This is archived by aligning the angular momentum of all stars along to the z-axis. The angular momentum $\mathbf{I}$ can be calculated by

$$\mathbf{I} = \sum_{i=1}^{N} m_i \mathbf{r}_i \times \mathbf{v}_i \tag{4.2}$$

or written for each coordinate

$$\mathbf{I}_x = \sum_{i=1}^{N} m_i \cdot (\mathbf{r}_{y,i} \cdot \mathbf{v}_{z,i} - \mathbf{r}_{z,i} \cdot \mathbf{v}_{y,i}) \tag{4.3}$$

$$\mathbf{I}_y = \sum_{i=1}^{N} m_i \cdot (\mathbf{r}_{z,i} \cdot \mathbf{v}_{x,i} - \mathbf{r}_{x,i} \cdot \mathbf{v}_{z,i}) \tag{4.4}$$

$$\mathbf{I}_z = \sum_{i=1}^{N} m_i \cdot (\mathbf{r}_{x,i} \cdot \mathbf{v}_{y,i} - \mathbf{r}_{y,i} \cdot \mathbf{v}_{x,i}). \tag{4.5}$$

The angular momentum is then normalized to a vector of length 1, $\mathbf{I}_0 = \mathbf{I}/I$. The angles used to transform $\mathbf{I}_0$ along the z-axis can be calculated:

$$\alpha = \arctan \frac{\mathbf{I}_{0,y}}{\mathbf{I}_{0,z}} \tag{4.6}$$

$$\beta = -\arctan \frac{\sqrt{\mathbf{I}_{0,x}^2 + \mathbf{I}_{0,y}^2}}{\mathbf{I}_{0,y}^2} \tag{4.7}$$

Here, α is the angle between the projection of $\mathbf{I}_0$ in the xy-plane and β the angle between $\mathbf{I}_0$ and the z-axis. To perform the alignment, $\mathbf{I}_0$ first needs to be rotated by $-\alpha$ around the z-axis and then by β around the y-axis. This can be archived by applying the following two rotation matrices

$$\mathbf{R}_z = \begin{pmatrix} \cos\alpha & \sin\alpha & 0 \\ -\sin\alpha & \cos\alpha & 0 \\ 0 & 0 & 1 \end{pmatrix} \tag{4.8}$$

$$\mathbf{R}_y = \begin{pmatrix} \cos\beta & 0 & \sin\beta \\ 0 & 1 & 0 \\ -\sin\beta & 0 & \cos\beta \end{pmatrix} \tag{4.9}$$

on all positions $\mathbf{r}_i$. As the whole galaxy has to be aligned, the rotations are performed on the dark matter and gas particles as well: $\mathbf{r}_{\mathrm{rot},i} = \mathbf{R}_y \mathbf{R}_z \mathbf{r}_i$.

One example for a rotated galaxy can be seen in Figure 4.1. In contrast to Figure 3.1, all stars are shown in blue, not only stars belonging to the disk. In black and in green, dark matter and gas particles are shown. One can see that the galaxy is indeed aligned to the z-axis in the stellar component, but slightly twisted in the gas component.

For comparison, a 10:1 merger is shown in Figure 4.2. The galaxy is still a disk, but disturbed, especially in the gas component, with a twisted and puffed-up disk.

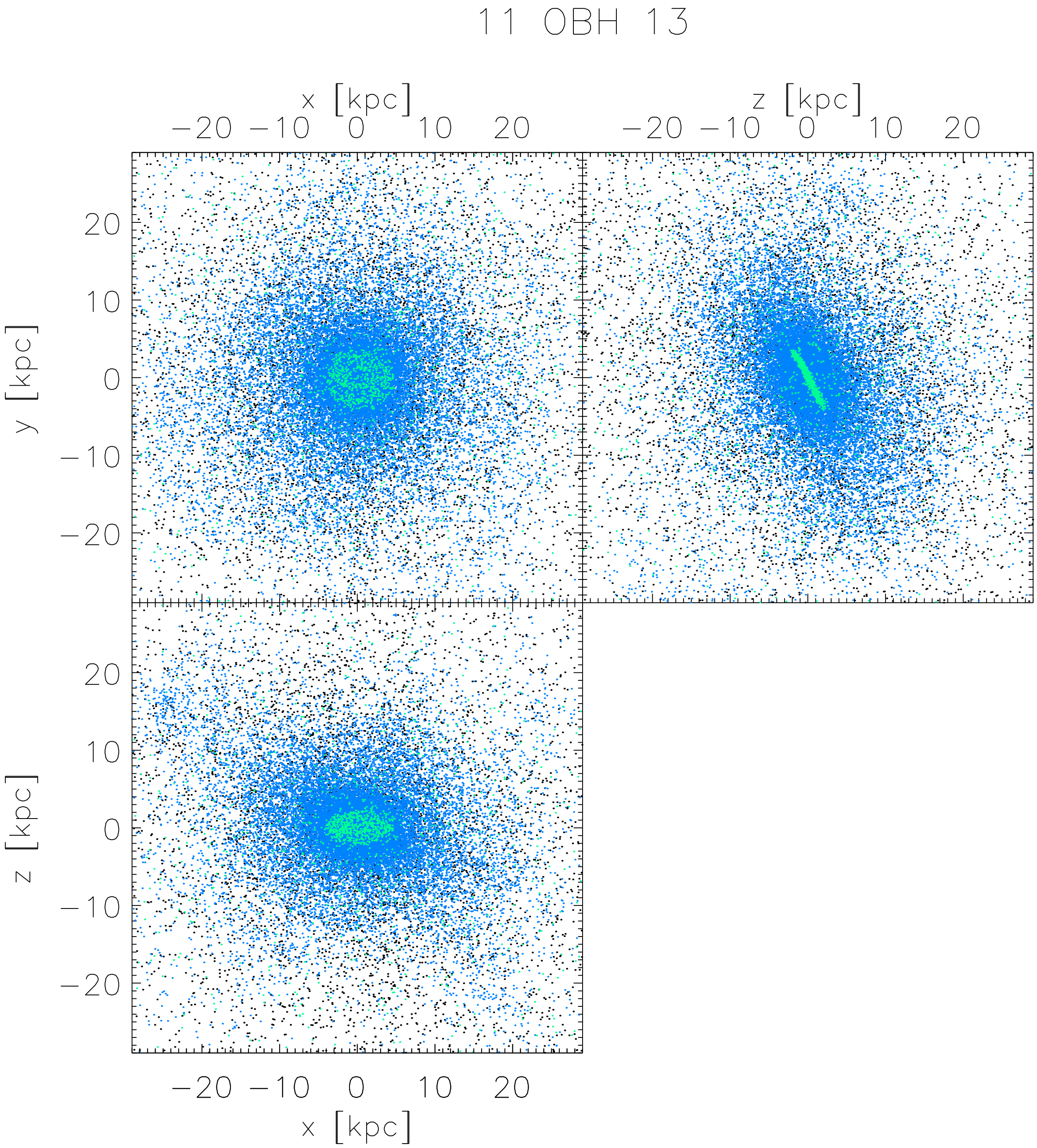

Figure 4.1: Appearance of the resulting elliptical galaxy 11 OBH 13. The components are plotted in different colors: dark matter (black), stars (blue) and gas (green). For a better view, every 20th particle is shown in this figure.

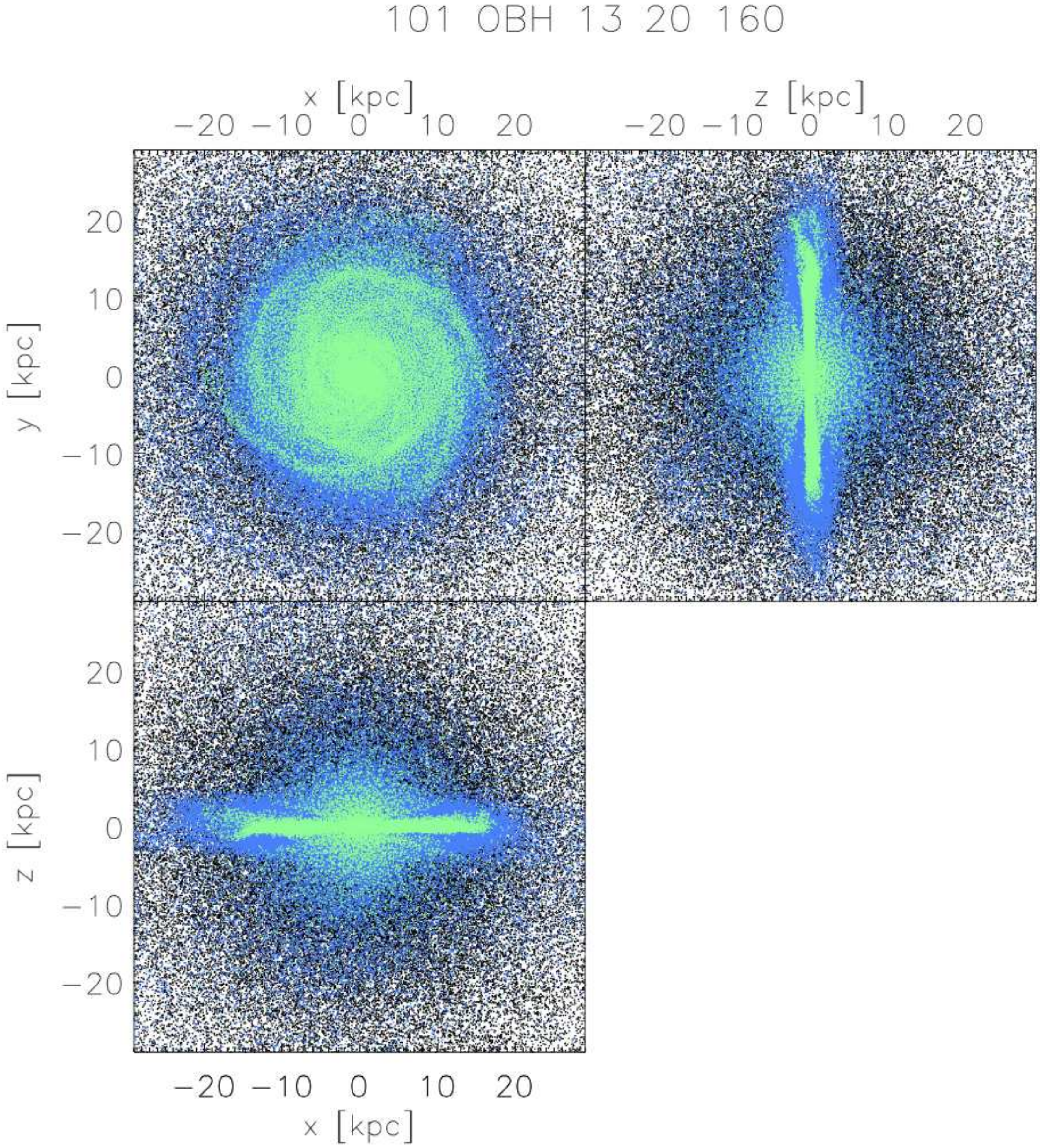

Figure 4.2: Appearance of the resulting elliptical galaxy 101 OBH 13 20 160. The components are plotted in different colors as in Figure 4.1.

4.1.1 Density Profiles

One important basic property of a galaxy is its density. Elliptical galaxies are gas poor, therefore the density is dominated by stars in the inner and dark matter in the outer regions. In the simulations, we calculate the density in terms of equal-number-bins as a function of radius. With $\rho(r) = M(r)/V(r)$ one gets for spherical shells

$$\rho(r) = \frac{N \cdot m_i}{\frac{4\pi}{3}(r_{\max}^3 - r_{\min}^3)}. \tag{4.10}$$

Each spherical shell contains $N = 2000$ particles. The volume is calculated as the difference of two spheres, the bigger one with radius $r_{\max}$, the radius of the Nth particle in the bin, the smaller one with radius $r_{\min}$, the radius of the Nth particle in the shell of the previous bin. m_i is the mass of one particle.

In Figure 4.3, the densities of stars (blue), gas (green) and dark matter (black) are shown for the elliptical 11 OBH 13. The density profile is indeed dominated by stars in the inner few kpc, moving out to larger radii, the dark matter becomes the dominant. The gas component drops after the inner few kpc to a tiny contribution.

The densities of all spheroids in Sample P are shown in Figure 4.4 with the same color-coding. Except for 31 O8BH 13, whose progenitors have a gas fraction of 80%, the density is dominated by stars in inner and dark matter in the outer parts of the elliptical and the gas content is negligible. In addition, I show the density profile of one of the galaxies from sample A, 11 OBH A02 20 160, in Figure 4.5. The remaining density profiles are shown in the Attachments.

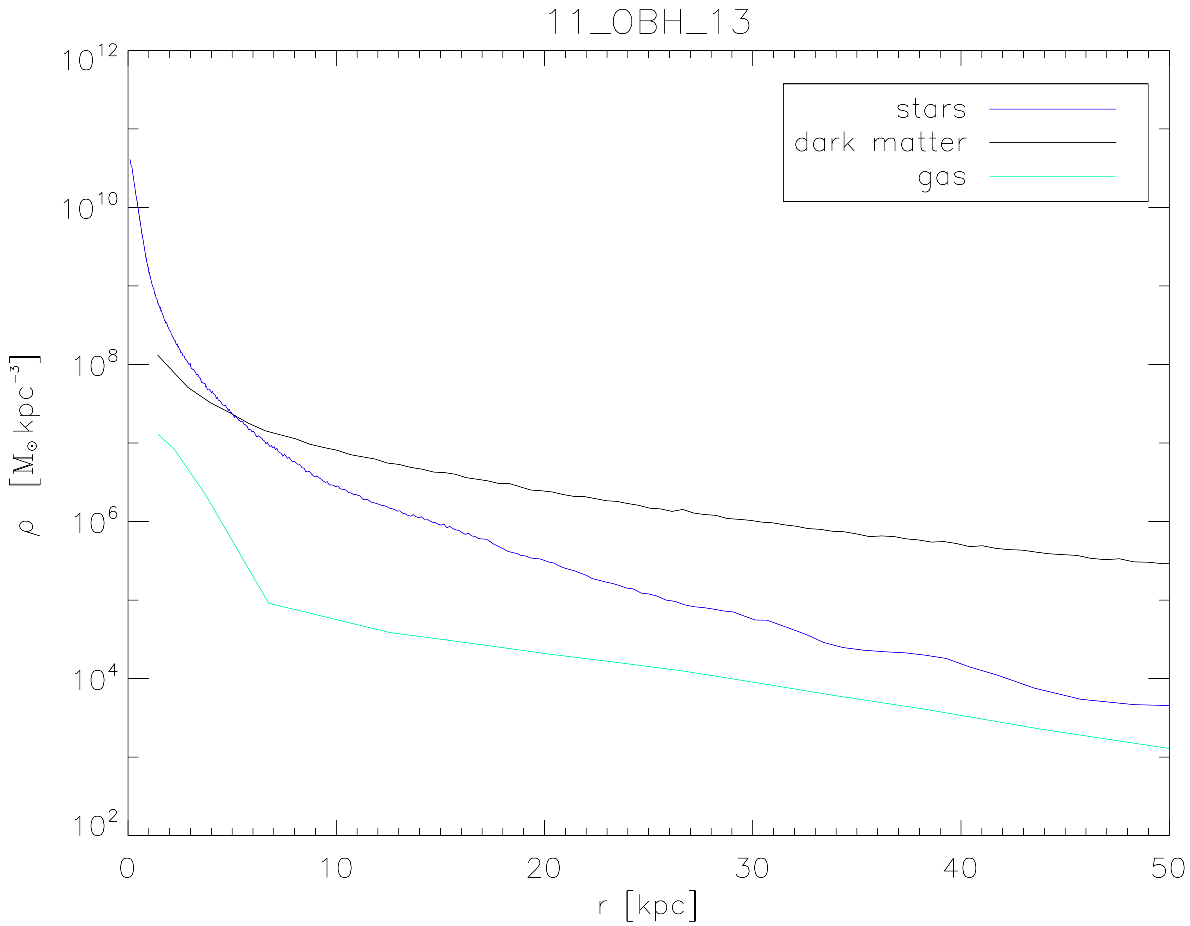

Figure 4.3: Density of 11 OBH 13 as a function of radius. Different components are shown in different colors: stars (blue), gas (green) and dark matter (black). The density is shown 3 Gyrs after the start of the simulation.

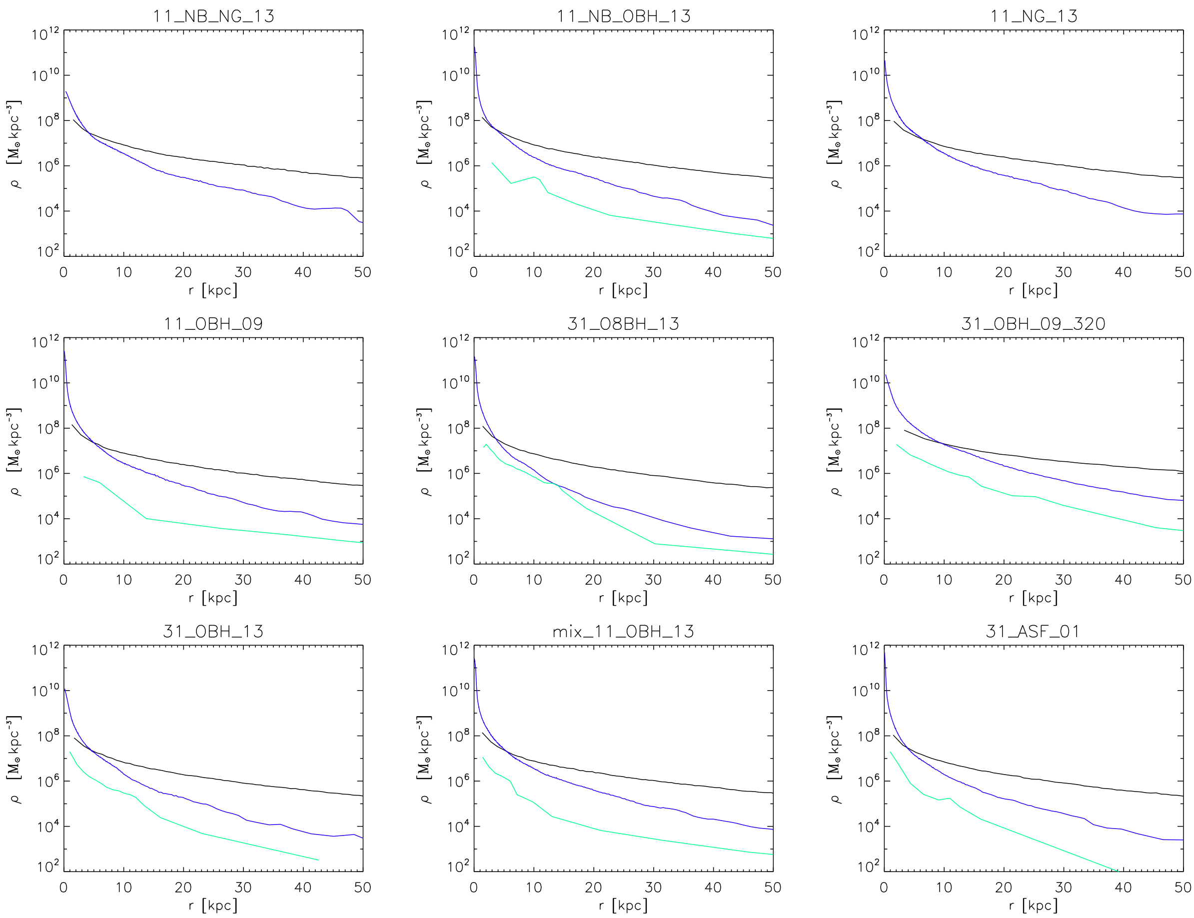

Figure 4.4: Density of all other spheroids in Sample P with the same color coding as in Figure 4.3. The densities are shown at 3 Gyrs after the simulation start as well.

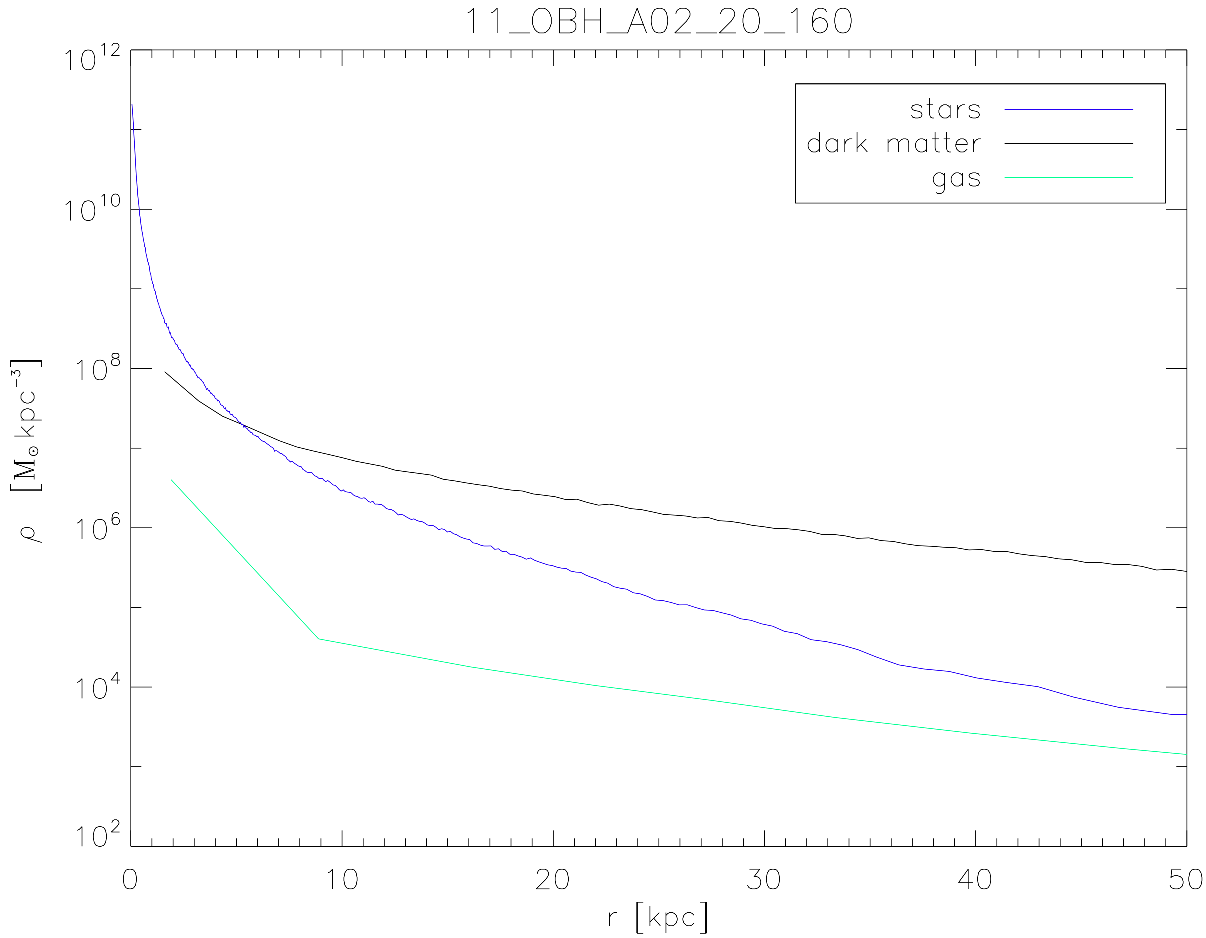

Figure 4.5: Density plot of 11 OBH A02 20 160 of Sample A with the same color coding as in Figure 4.3. The density is shown at 3 Gyrs after the simulation start as well.

4.1.2 Mass Profiles

Similar to the density profiles, the mass profiles of the ellipticals can be calculated. Therefore, the mass $M(<r)$ contained in radius r is added up and shown as a function of radius by integrating the density over the volume element:

$$M(<r) = \int_0^r \rho(r)\mathrm{d}^3r. \tag{4.11}$$

As we have discrete values, the integral is replaced by a sum. Figure 4.6 shows the mass profile for 11 OBH 13.

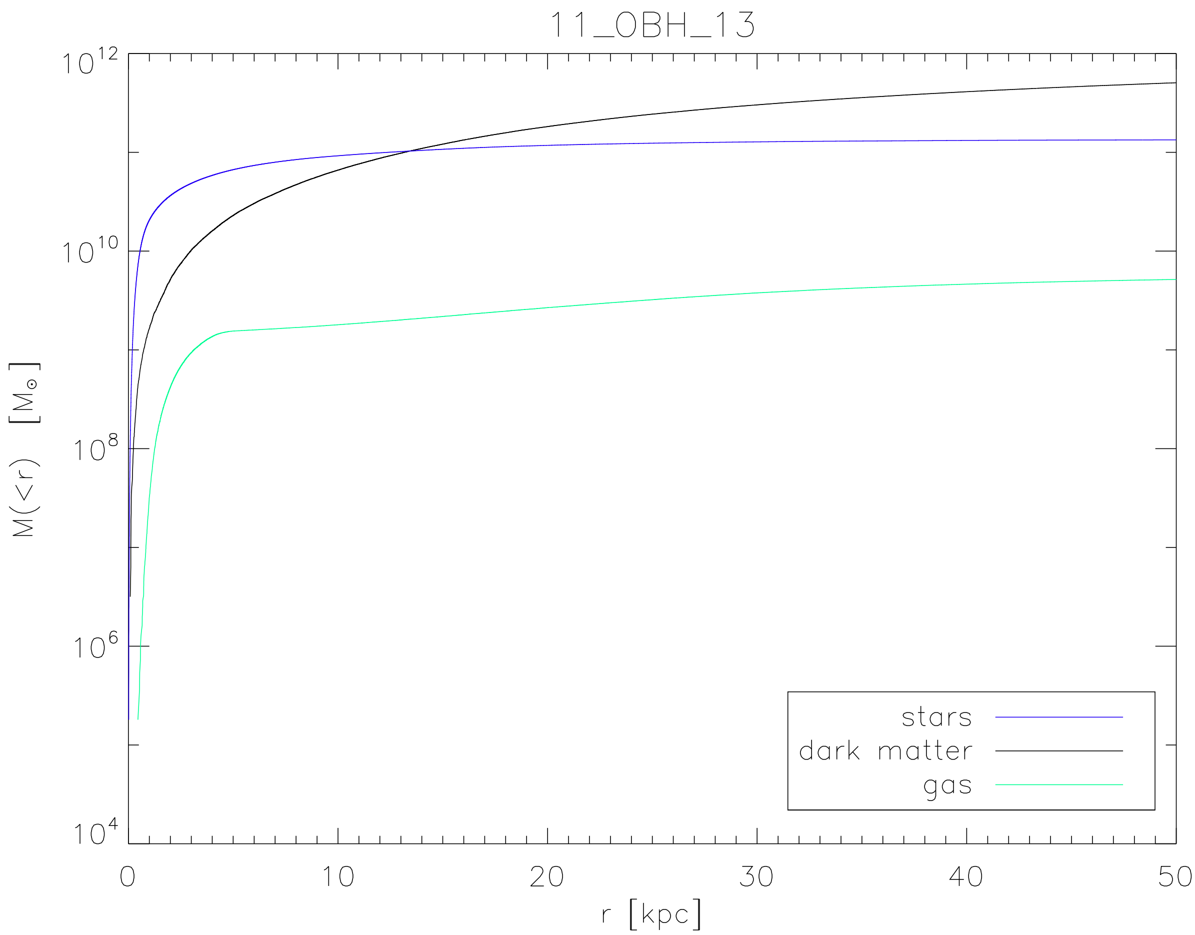

Figure 4.6: Mass plot for 11 OBH 13 with the same color coding as in Figure 4.3. The mass profile is shown at 3Gyrs after the simulation start.

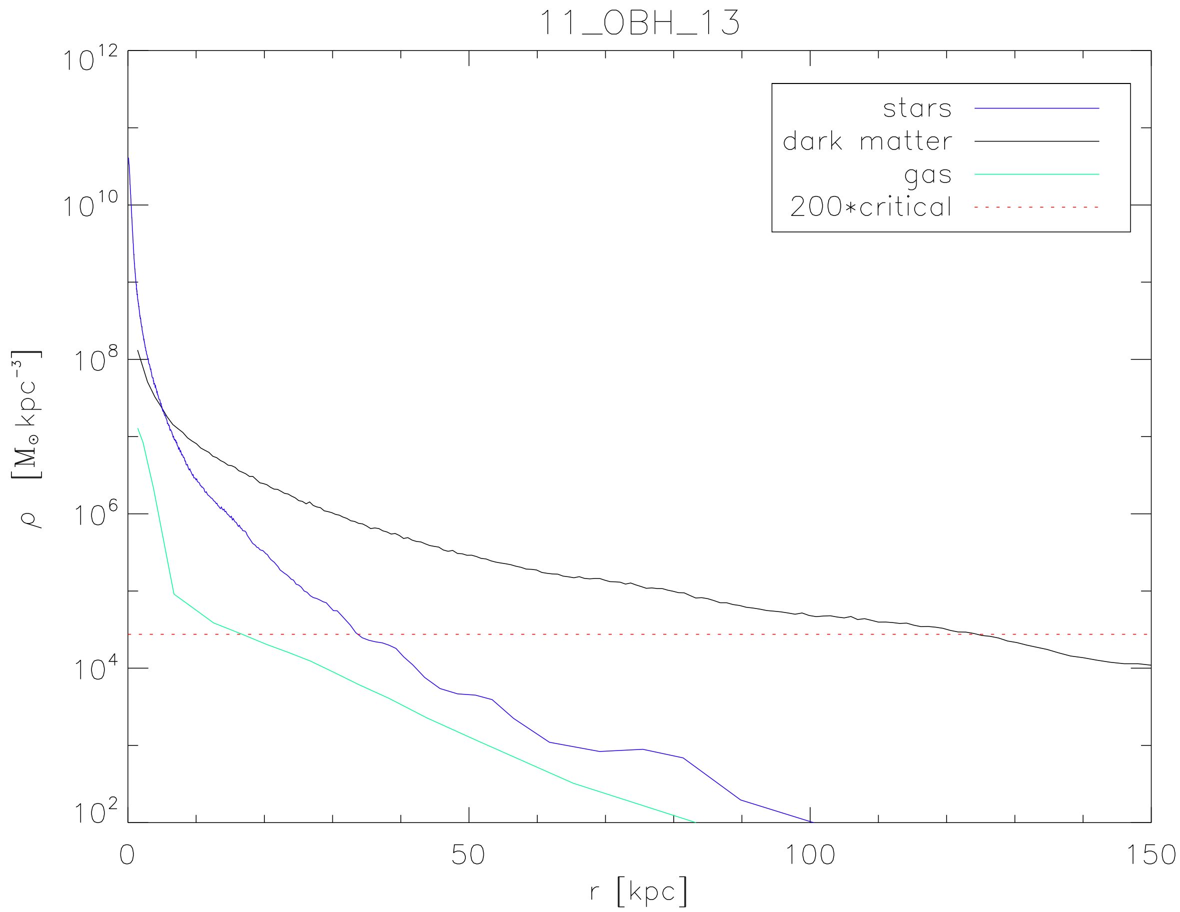

Figure 4.7: Density plot of 11 OBH 13 out to large radii. At the intersection of the black line (dark matter) and the red dotted line ($200 \cdot \rho_{\mathrm{crit}}$), we find the virial radius.

4.1.3 Virial Radius and Effective Radius

With the density profiles, the virial radius can be determined. Here, we define the virial radius to be the radius at which the density drops below $200 \cdot \rho_{\mathrm{crit}}$, where $\rho_{\mathrm{crit}} = 1.375 \cdot 10^2\, M_\odot\, \mathrm{kpc}^{-3}$ is the critical density of the universe.

In Figure 4.7, the density profile is shown out to large radii, where the dark matter is the only component contributing to the density. At the intersection of $200 \cdot \rho_{\mathrm{crit}}$ and the density, at about 128 kpc, the virial radius is found.

Like Remus et al. (2013) and Oser et al. (2010), the inner elliptical is defined in the inner 10% of the virial radius. Therefore, the stellar mass M_{stars} is calculated by adding up the stellar particle masses out to the radius $0.1 \cdot R_{vir}$.

The effective radius usually is defined as the half-light-radius from observations. In the simulation, there is no measurable light, but matter. Assuming a constant mass to light ratio, the effective radius is defined as the radius enclosing half of the stellar mass inside

Elliptical	R_{vir} [kpc]	$M^{\star}_{vir}$ [$10^{10}\,M_{\odot}$]	$M^{\star}_{10\%}$ [$10^{10}\,M_{\odot}$]	$R_{\rm eff}$ [kpc]
11 NB NG 13	132.5	10.80	7.25	8.48
11 NB OBH 13	129.5	10.28	7.40	6.15
11 NG 13	129.4	14.32	10.09	6.76
11 OBH 09	129.1	13.71	10.26	5.02
11 OBH 13	128.3	13.63	10.10	5.20
31 ASF 01	111.9	9.17	6.83	4.59
31 O8BH 13	114.3	7.76	6.76	2.56
31 OBH 09 320	227.1	73.55	56.12	10.42
31 OBH 13	116	8.94	6.89	5.22
mix 11 OBH 13	134	15.99	11.24	6.32
11 OBH 01 20 160	125.9	13.82	10.00	5.28
11 OBH A02 20 160	124.2	13.30	9.48	5.92
11 OBH A03 20 160	124.0	13.87	9.83	5.62
11 OBH A04 20 160	125.1	13.24	9.37	6.15
31 OBH 01 20 160	108.6	9.04	6.54	4.65
31 OBH 13 20 160	86.6	8.78	5.98	5.19
31 OBH A02 20 160	110.2	8.88	6.72	4.94
101 OBH 09 20 160	105.2	7.15	5.55	4.62
101 OBH 13 20 160	104.9	7.17	5.46	4.76

Table 4.1: Basis properties of the resulting ellipticals formed by major mergers.

the virial radius.

In Table 4.2, I list these properties for all Major Merger simulations from sample P and A. In addition, I also give the stellar mass within the virial radius.

4.2 Ellipticals from Cosmological Resimulated Galaxies

The elliptical galaxies formed by a cosmological zoom resimulation are treated as the ones formed in a major merger simulation. The center of mass is calculated and the galaxy is also aligned to the angular momentum.

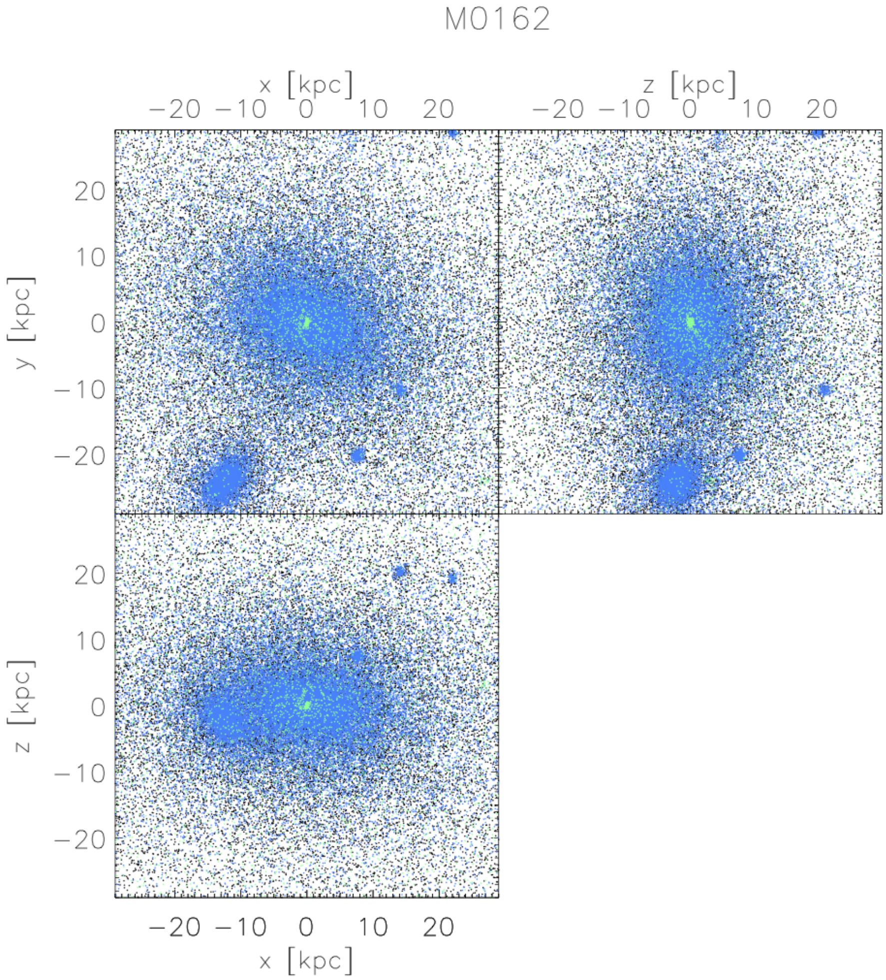

Figure 4.8: Appearance of the resulting elliptical galaxy M0162. The components are plotted in different colors as in Figure 4.1.

Here, I show one example of a galaxy, M0162 in Figure 4.8. One can immediately see the main problem with the ellipticals produced by the Cosmological Simulation: there are a lot of satellites in the halo which disturb the kinematics. In this example, there is at least one big and two smaller satellites within the central 30 kpc.

4.2.1 Density Profiles

Similarly to the Major Merger case, density profiles can be created for the Cosmological Zoom galaxies as well. Here, the density is also dominated by the dark matter in the outer parts and by the stellar component in the inner region. In Figure 4.9, the density profile for M0162, one can see that the big satellite causes a increased stellar density at about 27 kpc. The gas component is very small.

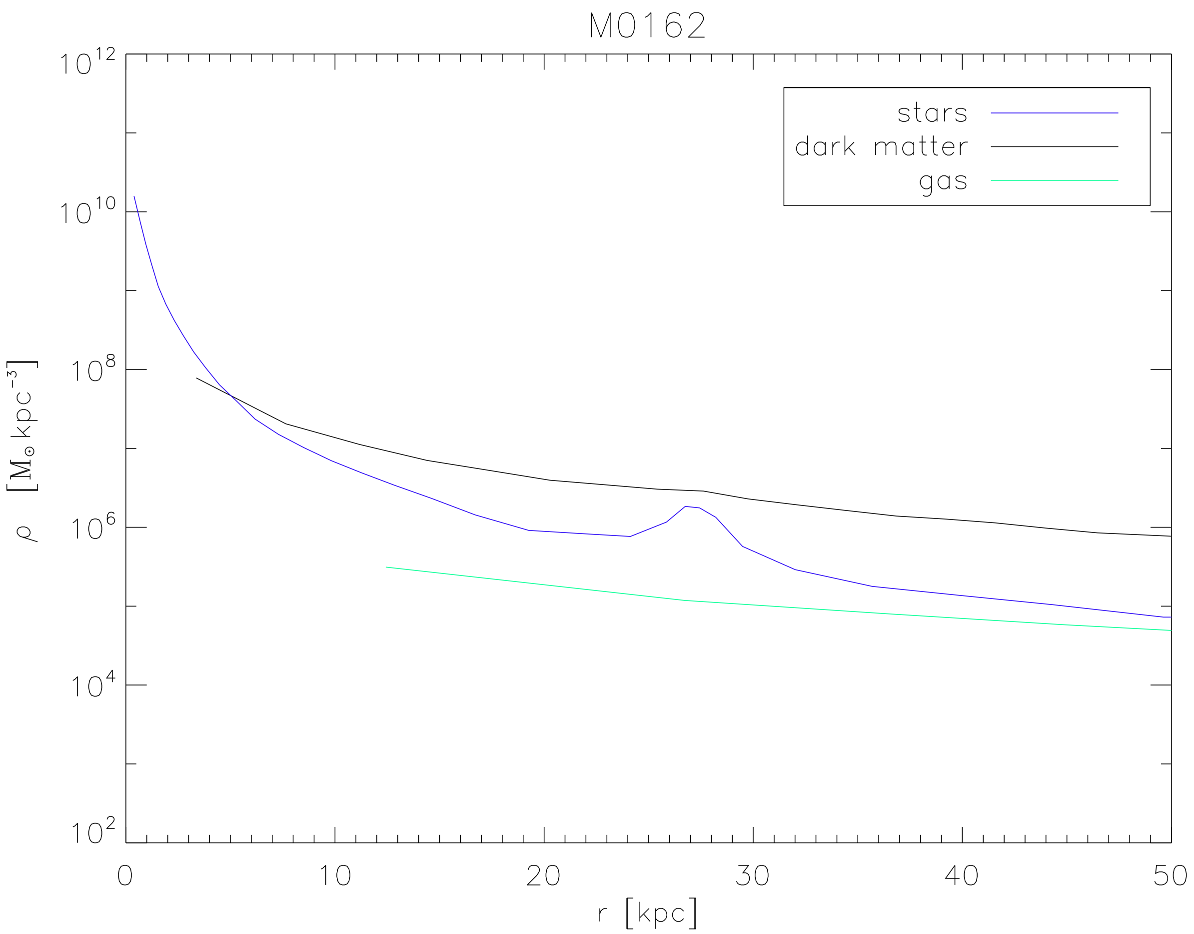

Figure 4.9: Density profile of the resulting elliptical galaxy M0162. The components are plotted in different colors as in Figure 4.1.

4.2.2 Mass Profiles

In Figure 4.10, I show the mass profile for the galaxy M0162. Due to satellites, the stellar mass increases even in the outer parts and does not reach a constant value quickly.

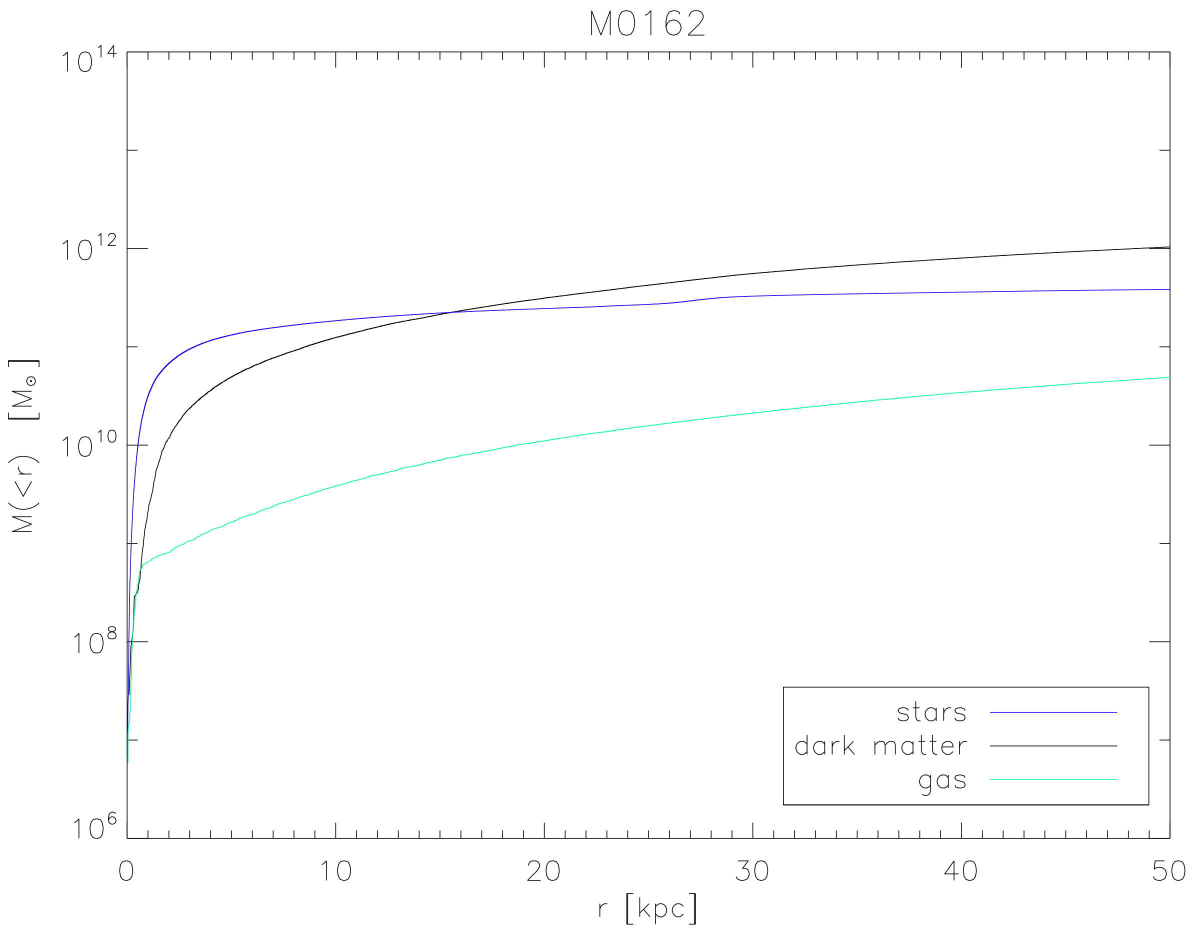

Figure 4.10: Mass profile of the resulting elliptical galaxy M0162. The components are plotted in different colors as in Figure 4.1.

4.2.3 Virial Radius and Effective Radius

Similar to the Major Merger simulation, one can determine the virial radius, the mass enclosed in 10% of the virial radius and the effective radius. But due to the satellite problem, the total stellar mass is estimated to high and therefore, the effective radius is too big. To get a slightly better approximation, I introduce a second effective radius. This second effective radius $R_{\text{eff},2}$ is defined as the radius which encloses half of the mass inside 10% of R_{vir}, $M^{\star}_{10\%}$. I list these properties for all ellipticals produced by Cosmological Zoom Simulations in Table **??**

Elliptical	Resolution	R_{vir} [kpc]	$M^{\star}_{vir}$ [$10^{10}\,M_{\odot}$]	$M^{\star}_{10\%}$ [$10^{10}\,M_{\odot}$]	$R_{\rm eff}$ [kpc]	$R_{\rm eff,2}$ [kpc]
M0004	2x	522.1	659.79	203.34	135.30	15.06
M0040	2x	385.2	183.59	41.10	201.29	8.51
M0053	2x	296.0	134.91	51.14	54.11	7.14
M0069	2x	316.7	100.86	40.46	64.13	5.66
M0089	2x	267.7	90.69	37.84	39.00	6.15
M0094	2x	253.4	82.40	37.96	30.27	4.63
M0125	2x	254.7	71.92	34.54	28.40	6.06
M0162	2x	219.6	54.50	25.33	25.32	4.65
M0163	2x	235.6	60.56	27.26	30.48	6.38
M0175	2x	232.8	58.72	30.42	21.37	5.07
M0189	2x	242.4	41.36	22.58	16.99	2.92
M0190	2x	210.6	47.76	25.58	17.36	4.58
M0204	2x	209.2	47.18	21.10	27.87	3.98
M0209	2x	242.0	44.02	17.84	55.45	3.20
M0215	2x	197.9	44.46	22.51	18.95	3.69
M0204	4x	196.7	50.04	22.90	24.90	3.77
M0227	4x	204.4	60.01	26.03	28.94	3.12
M0408	4x	154.7	24.44	12.48	14.52	2.02
M0501	4x	159.3	25.00	14.55	9.01	2.50
M0616	4x	145.5	23.41	15.16	7.56	4.11
M0664	4x	149.4	19.86	10.79	10.66	2.23
M0858	4x	131.9	8.70	3.15	25.20	3.40
M0959	4x	135.8	11.49	7.28	6.82	2.13
M0977	4x	96.0	7.19	5.24	3.68	2.11
M1196	4x	113.7	11.27	8.55	2.98	2.08
M1646	4x	112.5	9.22	6.21	3.50	1.90
M2283	4x	44.7	5.10	3.01	2.57	1.29
M4323	4x	38.5	3.93	2.64	1.97	1.36
M6782	4x	31.4	3.31	2.30	1.54	1.13
M6782	8x	46.1	1.56	1.39	1.23	1.02

Table 4.2: Basis properties of the resulting ellipticals formed by major mergers.

5 The Mystery of the σ-bump

In this chapter, I will present a possible tracer for major mergers, the σ-bump. It has first been found in simulations, but some observations seem to show a feature like the σ-bump as well. These findings have been published as Schauer et al. (2014). The study is based on simulations by Johansson et al. (2009a,b) described as sample P in the prior chapter.

5.1 The Velocity Dispersion

The velocity dispersion σ is the second momentum of the velocity after the mean velocity. Here, we are interested in the intrinsic (or total) velocity dispersion of all three coordinates, calculated separately for stars, gas and dark matter.

In a first step, the velocity dispersion is calculated for each Cartesian component i separately as a function of the radius $\sigma_i(r)$ $(i = x, y, z)$. For this, we sort the particles into equal radius bins with a binwidth of 0.1 kpc. The number of particles is a bin is denoted by N:

$$\sigma_i(r) = \sqrt{\frac{\sum v_i(r)^2}{N} - \left(\frac{\sum v_i(r)}{N}\right)^2}. \tag{5.1}$$

The intrinsic velocity dispersion σ is the Euclidean norm of the x, y and z component:

$$\sigma = \sqrt{\sigma_1^2 + \sigma_2^2 + \sigma_3^2}. \tag{5.2}$$

'Observations have shown that the projected velocity dispersion (= root mean squared velocity) of the stellar component can in general be well-fitted by a power-law (Douglas et al., 2007; Napolitano et al., 2009)' (Schauer et al., 2014, section 3). Therefore, a power law is fitted to the velocity dispersion with exponent β

$$\sigma \propto r^{\beta} \tag{5.3}$$

out to a radius of 50 kpc.

5.2 The σ-bump

Figure 5.1 shows the velocity dispersion as a function of radius of 11 OBH 13. One can see that in the stellar component, the velocity dispersion follows the power-law $\sigma_{\text{fit}} = 365.3 \cdot r^{-0.20}$ nicely except for a region between one and three R_{eff}. This deviation is

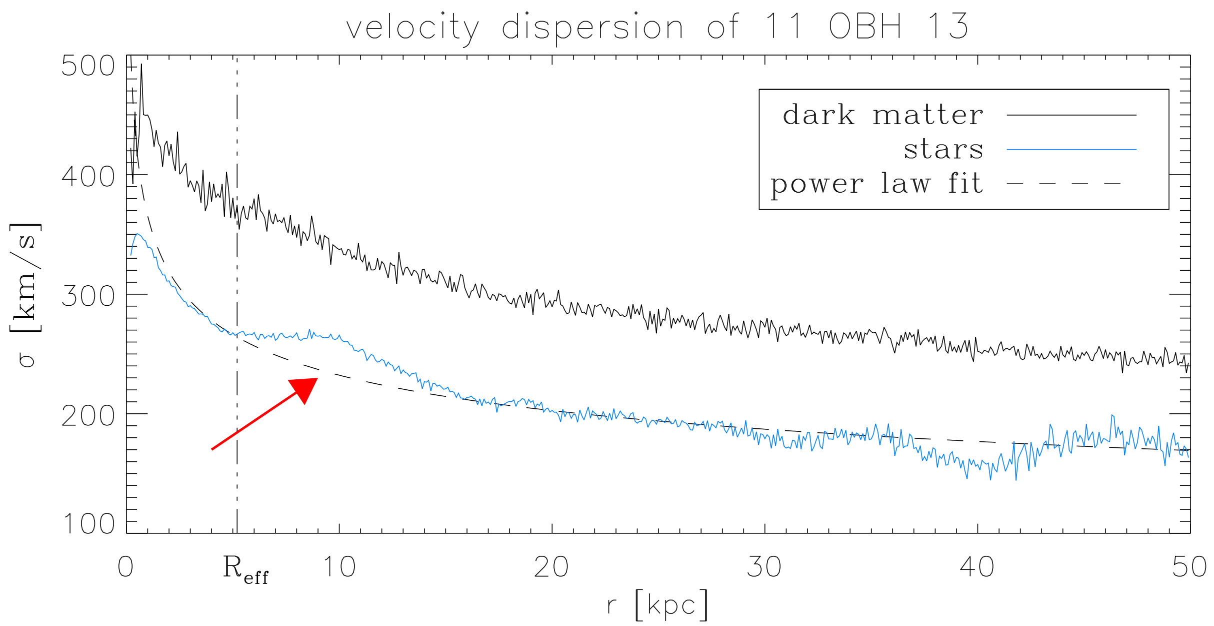

Figure 5.1: Stellar (black) and dark matter (blue) intrinsic velocity dispersion as function of radius for galaxy 11 OBH 13. For the stellar component, the power law fit is included (black dashed curve). The σ-bump (red arrow) as a positive deviation from a power-law behavior appears only in the stellar component (compare Schauer et al. (2014), Figure 1, upper panel).

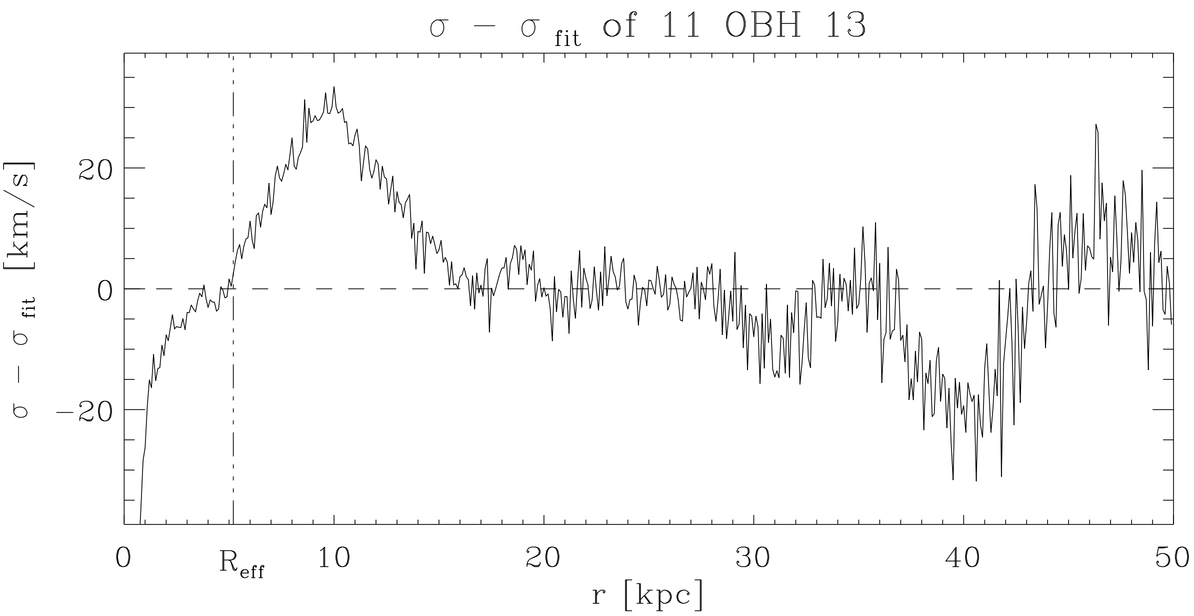

Figure 5.2: Difference of the intrinsic stellar velocity dispersion and its power law fit as function of radius for galaxy 11 OBH 13. The deviation resembles a triangle.

indicated with a red arrow and is referred to as the 'σ-bump'. To further emphasize the σ-bump, one can plot the difference of the velocity dispersion and its fitted power law. The deviation resembles a triangle, shown in Figure 5.2 for 11 OBH 13.

The σ-bump does not depend on the resolution. Figure 5.3 shows the same physical properties as Figure 5.1, but is computed with equal number bins with more than 1500 particles per bin. One can see that the velocity dispersions are the same in both figures, but the power-law fit is worse with the equal number bins because the inner parts with too low velocity dispersion have a lot of bins and are thus overemphasized.

This σ-bump is different from other features like shells which vary with time or numerical artifacts. The velocity dispersion is low in the inner two kpc, which is populated by bulge stars of the progenitor stars of the galaxies. They are bound in the centers of the galaxies by a deep gravitational potential. 'Shells can form in major mergers, e.g. described by Cooper et al. (2011), leading to an ejection of stars in density waves (Schweizer, 1986). Therefore, the velocity dispersion varies at the radii $30 - 50$ kpc where shells are present' (Schauer et al., 2014).

Figure 5.4 shows the velocity dispersion of galaxy 11 OBH 13 for different time steps to emphasize the difference of the σ-bump to time dependant shells. The velocity dispersion at 1.7 Gyrs (red line) and therefore only 0.2 Gyrs after the merger, where the galaxy has not relaxed, displays many deviations from the power law. At 2.0 Gyrs (yellow line), the deviations outside three effective radii decrease in height and move outwards. For later timesteps (3, 6 and 9 Gyrs in green, blue and black) the σ-bump stays unaltered, while all

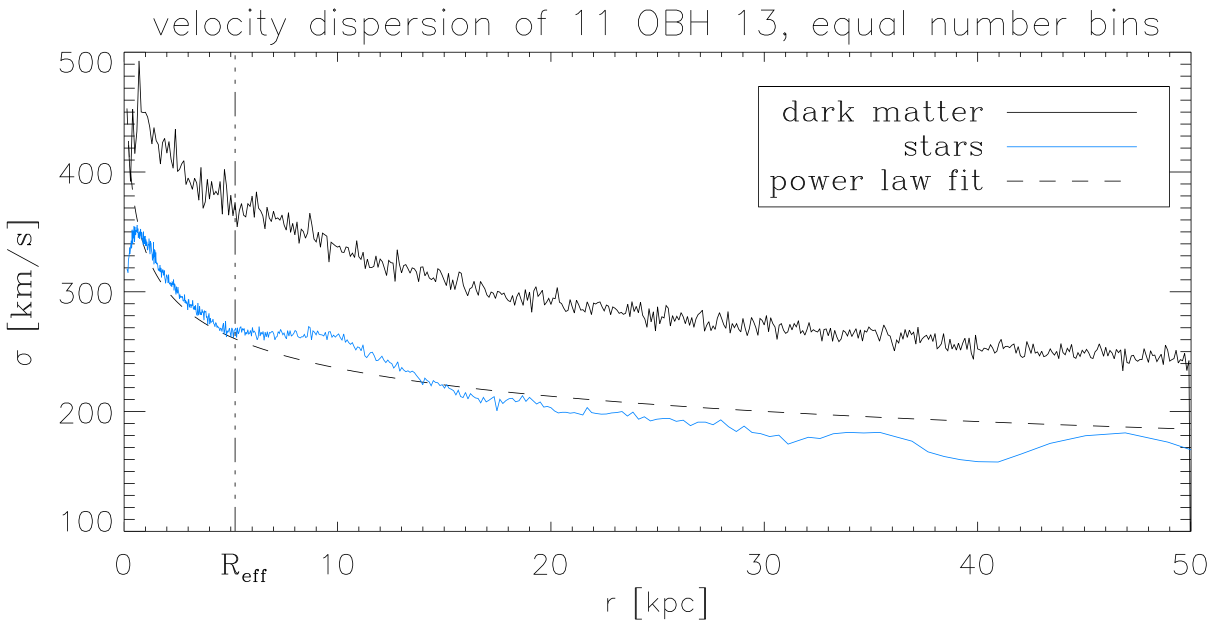

Figure 5.3: Velocity dispersion and σ-bump of 11 OBH 13 with equal number bins.

other deviations vanish.

The σ-bump is present in the whole sample P, but to different extent. 1:1 merger show the bump more prominently than 3:1 merger. In Figure 5.5, the velocity dispersions as well as their deviations to the corresponding power law fit are shown at 3 Gyrs. The σ-bump is dependant on the orbit, as there is a difference in the 11 OBH 13 and the 11 OBH 09 ellipticals. The 31 ASF 01 elliptical with the retrograde G01 orbit shows a weak double-bump.

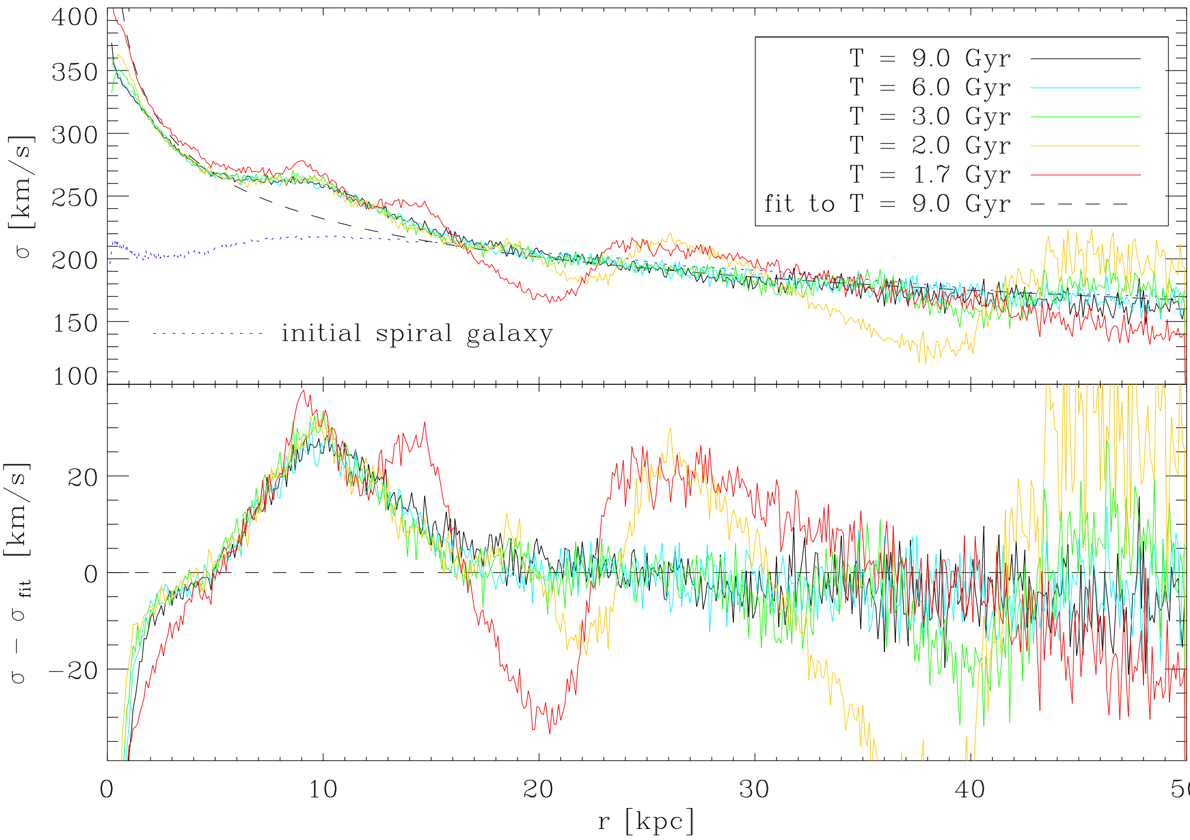

Figure 5.4: Upper panel: The intrinsic stellar velocity dispersion of the example galaxy against the radius. Different colors indicate different time steps of the simulation (merger encounter at 1.5 Gyrs). The intrinsic stellar velocity dispersion of the progenitor spiral galaxy is added (blue dashed line). Lower panel: Difference of the intrinsic stellar velocity dispersion to the corresponding power-law fit for different time steps (colors same as upper panel). Figure and description are taken from Schauer et al. (2014), Figure 3.

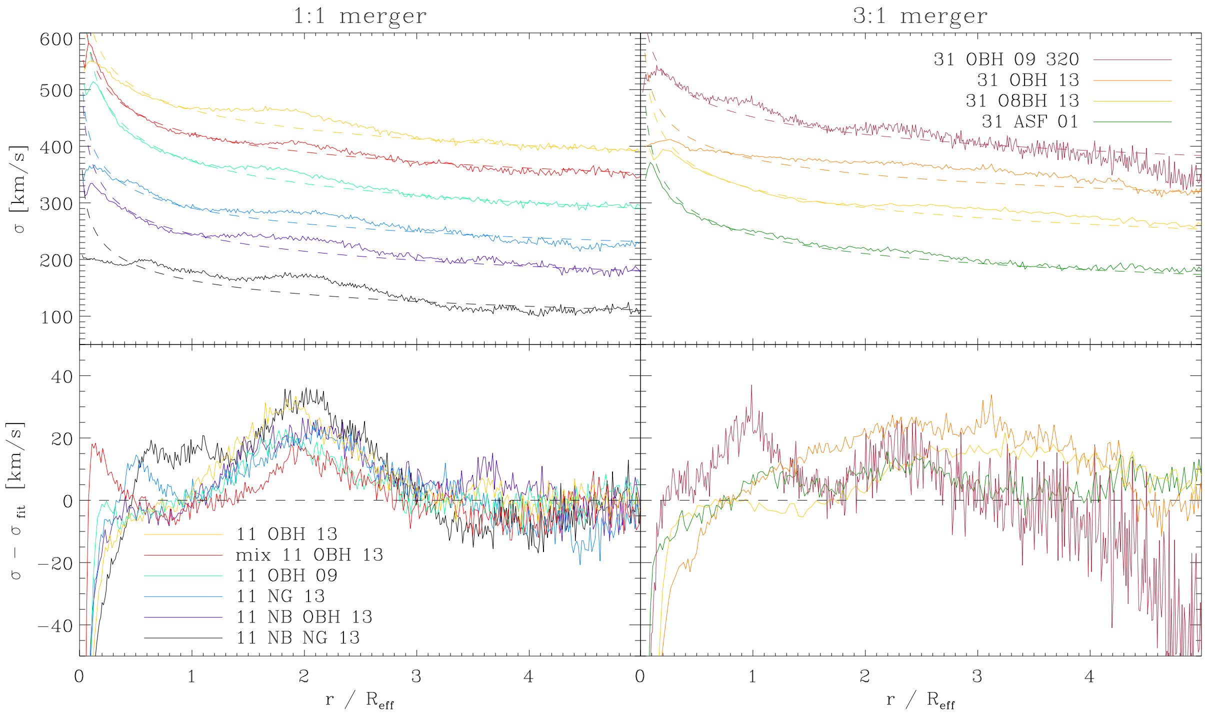

Figure 5.5: Velocity dispersion and σ-bump in the ten simulations of sample P. Left column: 1:1 mergers, right column: 3:1 mergers (all at 3 Gyrs). Upper panels: The velocity dispersion of the different spheroids (solid lines) and their corresponding power laws (dashed lines) as functions of the effective radius. For better readability, we shift the dispersion profiles for all mergers except 11 NB OBH 13, 31 ASF 01 and 31 O8BH 09 320 by multiples of 50 km/s. The lower panel displays the difference between the velocity dispersion and its best fit power-law. Figure and description taken from Schauer et al. (2014), Figure 2.

5.3 Comparison to Observations

'To compare our results to observations it is not sufficient to just consider the intrinsic stellar velocity dispersion, but also its projections. Figure 5.6 shows the line-of-sight velocity dispersion for different projections from face-on ($0°$) to edge-on ($90°$) in different colors against radius for our example galaxy, as well as the intrinsic velocity dispersion and its power-law fit. The σ-bump can be seen in all line-of-sight velocity projections, although with a somewhat lower relative amplitude, and should therefore be detectable by observations.

We compare our simulations with results from radial velocity measurements of PNe and red GCs in ETGs, as the red GCs are presumed to trace the field–star component of ETGs. We need these tracers to detect a decline in σ after 3 $R_{\rm eff}$ out to at least 4 $R_{\rm eff}$, as stellar data does not provide this information. We use published position and velocity measurements to calculate the velocity dispersion as a function of radial distance. For most of the observed galaxies currently available, the observational data sets are not sufficient: either the total sample of tracers contains fewer than 200 objects, or the data mainly trace radii at which we do not expect to see the σ-bump.

Pota et al. (2013) recently published the kinematics of a sample of globular clusters in 12 ETGs from a spectroscopic survey (see also Strader et al. 2011; Arnold et al. 2011; Foster et al. 2011). The sample of PNe data from Coccato et al. (2009) is of similar size, but here we focus on the sample of Pota et al. (2013). We find a σ-bump in four of the twelve galaxies (NGC 821, NGC 1407, NGC 3115, NGC 4278) from this sample, while three other galaxies (NGC 3377, NGC 4365 and NGC 4494) do not show a significant comparable feature but a constant or decreasing velocity dispersion. For the remaining five galaxies we cannot draw any firm conclusion as we are limited by low-number statistics (37 and 42 red GCs in NGCs 1400 and 2768, respectively, and 21 GCs in NGC 7457), the feature varies a lot with binsize (NGC 4486) or is observed at too large radii (NGC 5846). We include in Figure 5.6 the observed galaxies which most prominently show a σ-bump at the location of the σ-bump of our simulated galaxy 11 OBH 13:

For NGC 821, both PNe and red GCs trace a σ-bump behavior between 0.5 and 1.8 $R_{\rm eff}$ ($R_{\rm eff}$ = 5.79 kpc, PNe data from Coccato et al. 2009, GCs data from Pota et al. 2013, stellar data from Proctor et al. 2009; Forestell & Gebhardt 2010). It is an isolated E6 galaxy, with a velocity dispersion that generally shows a rapid decrease with radius (Romanowsky et al., 2003) and kinematic and photometric signatures of an edge-on stellar disk (Proctor et al., 2009).

The GCs data of NGC 3115 were first presented by Arnold et al. (2011). This S0-galaxy contains a chemically enriched and kinematically distinct stellar disk (Norris et al., 2006). The σ-bump can be seen in the range of 0.7 to 2.2 $R_{\rm eff}$ ($R_{\rm eff} = 3.87\,$kpc).

For NGC 4278 (GCs data from Pota et al. 2013, stellar data from van der Marel & Franx 1993) we observe a σ-bump in a large range: from 1.5 to 3.8 $R_{\rm eff}$ ($R_{\rm eff} = 2.58\,$kpc). This galaxy has a large HI disk and a dusty patch (Goudfrooij et al., 1994).

Additionally, we might have found a σ-bump feature in the galaxy NGC 4697. For this galaxy, two dataset of are available: 218 PNe from Méndez et al. (2009) and 531 PNe from

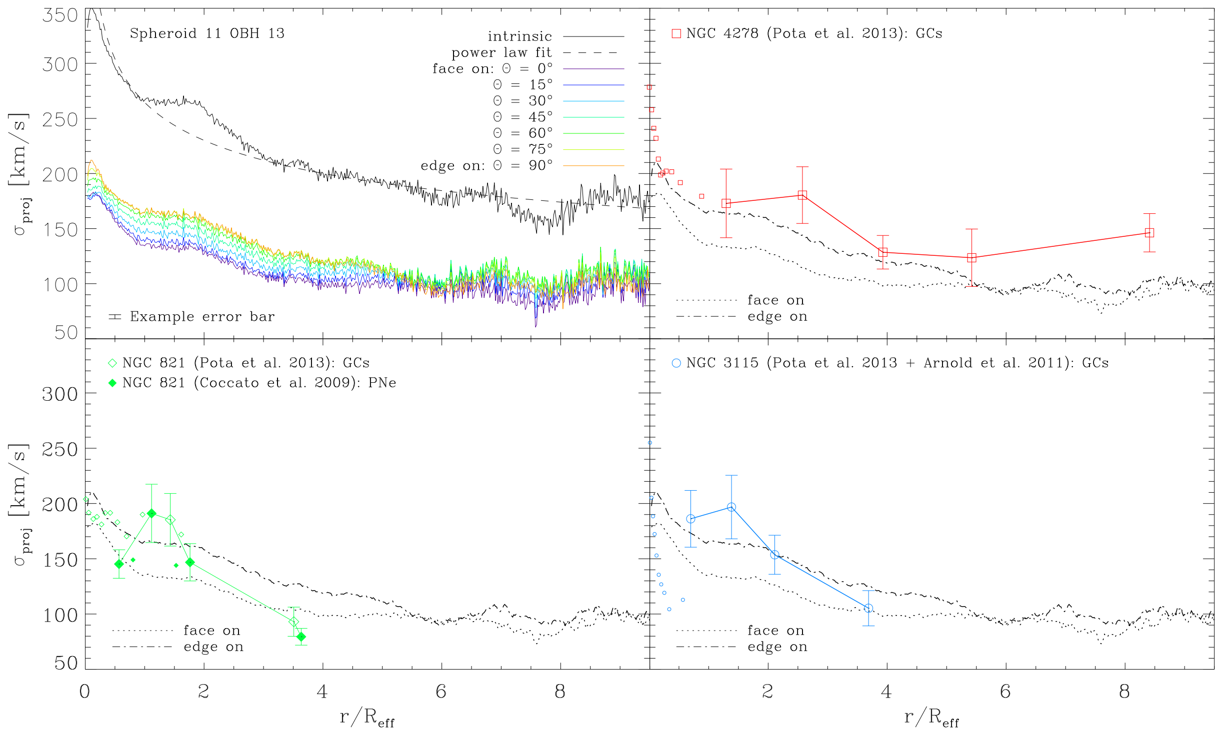

Figure 5.6: Upper left panel: The stellar velocity dispersion against the radius of example galaxy 11 OBH 13. Black line: intrinsic stellar component, black dashed line: a power law fit to the intrinsic stellar component, dark violet: face on projection, orange: edge on projection, other colors: projections at different angles. Other three panels: Observational data. Upper right panel: NGC 4278. Lower left panel: NGC 821. Lower right panel: NGC 3115. GCs and PNe are shown by large symbols, additional stellar data by small symbols of the same kind and color (stellar data for NGC 821 from Forestell & Gebhardt (2010) (open diamonds) and Proctor et al. (2009) (filled diamonds), for NGC 3115 from Norris et al. (2006), for NGC 4278 from van der Marel & Franx (1993). We include the face–on and edge–on projections of the simulated example galaxy as dotted and dash–dotted lines. Figure and figure description taken from Schauer et al. (2014), Figure 4.

Méndez et al. (2001, 2008).

The kinematic information covers the central area as well as the outer regions of the galaxy, showing a σ-bump behavior between 0.9 and 2.7 R_{eff} ($R_{\text{eff}} = 3.36\,\text{kpc}$, stellar data from Binney et al. 1990). NGC 4697 is an E4-5 galaxy with a stellar disk along the major axis (Carter, 1987; Goudfrooij et al., 1994) and at least two PNe subpopulations (Sambhus et al., 2006).

We thus conclude that the σ-bump is a feature that can be observed with tracers in the outer parts of ETGs in the stellar component, given a statistically significant number of tracers is available' (Schauer et al., 2014).

6 Explanations for the σ-bump

With the σ-bump, we have found a possible tracer for a major merger formation scenario of elliptical galaxies. In the chapter, I will examine the correlation of different parameters with the σ-bump.

6.1 Comparison to Cosmological Zoom Simulations

In Chapter 3, I have described not only the major merger simulations used in Schauer et al. (2014), but also a set of 30 ellipticals formed by cosmological zoom simulations. I will compare this second type of simulations with the major merger simulations.

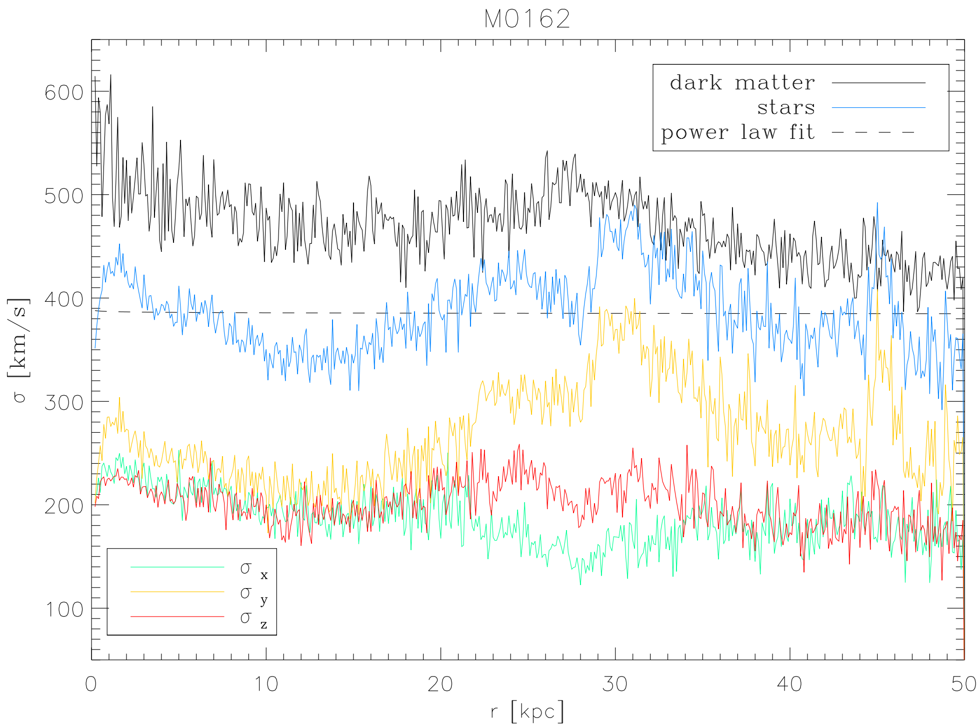

Figure 6.1: Velocity dispersion of M0162. The intrinsic stellar velocity dispersion (blue line) is shown together with its power law fit (black dashed line) and the dark matter velocity dispersion (black line). In addition, the Cartesian components of the stellar velocity dispersion are shown in green, yellow and red.

The velocity dispersion is calculated in the same way for the cosmological zoom simulations. In Figure 6.1, the stellar and dark matter component of the elliptical M0162 are displayed. In addition to the intrinsic stellar (blue line) and dark matter (black line) velocity dispersions, the Cartesian components of the stellar velocity dispersion are shown (green, yellow and red lines). M0162 is a typical elliptical of this simulation set and therefore used as a representative for the sample.

No σ-bump can be identified in this figure, the velocity dispersion is scattering a lot. A power-law fit is not reasonable. The velocity dispersion deviations are due to accreting satellites. This is emphasized by the Cartesian components: while the σ-bump was visible similarly in all components, the power-law deviations shown in this figure are mostly driven by one component, in this case primary by the σ_y component.

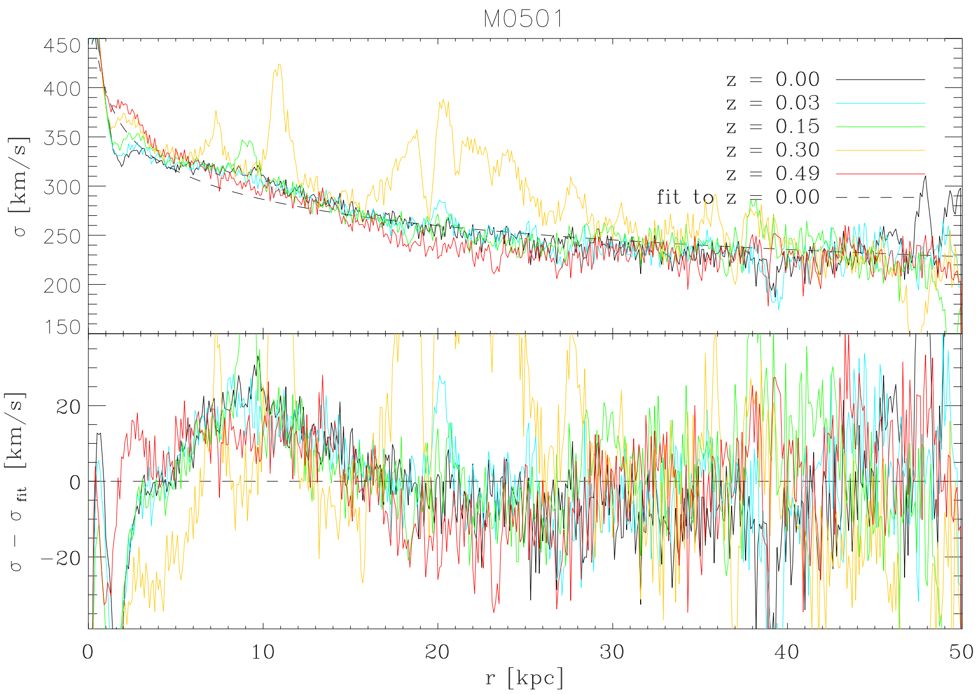

Figure 6.2: Velocity dispersion of M0501 for different redshifts.

One of the resimulated galaxies does indeed show a σ-bump: M0501. In Figure 6.2, the stellar velocity dispersion is shown for different redshifts. At the first shown redshift, $z = 0.49$, no σ-bump can be identified. This changes with a merger at $z = 0.30$, which causes big variations of the velocity dispersion. After this merger, the velocity dispersion does not change a lot in the inner 20 kpc. Depending on the method, the effective radius is calculated as 9.01 kpc or 2.5 kpc (compare section 4.2.3). Therefore, a σ-bump between approximately five and 18 kpc fits in the picture.

By visualizing the galaxy M0501 as shown in Figure 6.3, one immediately steps onto one feature: a gas ring (green). This is similar to the major merger galaxy 11 OBH 13, which also shows a gaseous disk in the center of the galaxy.

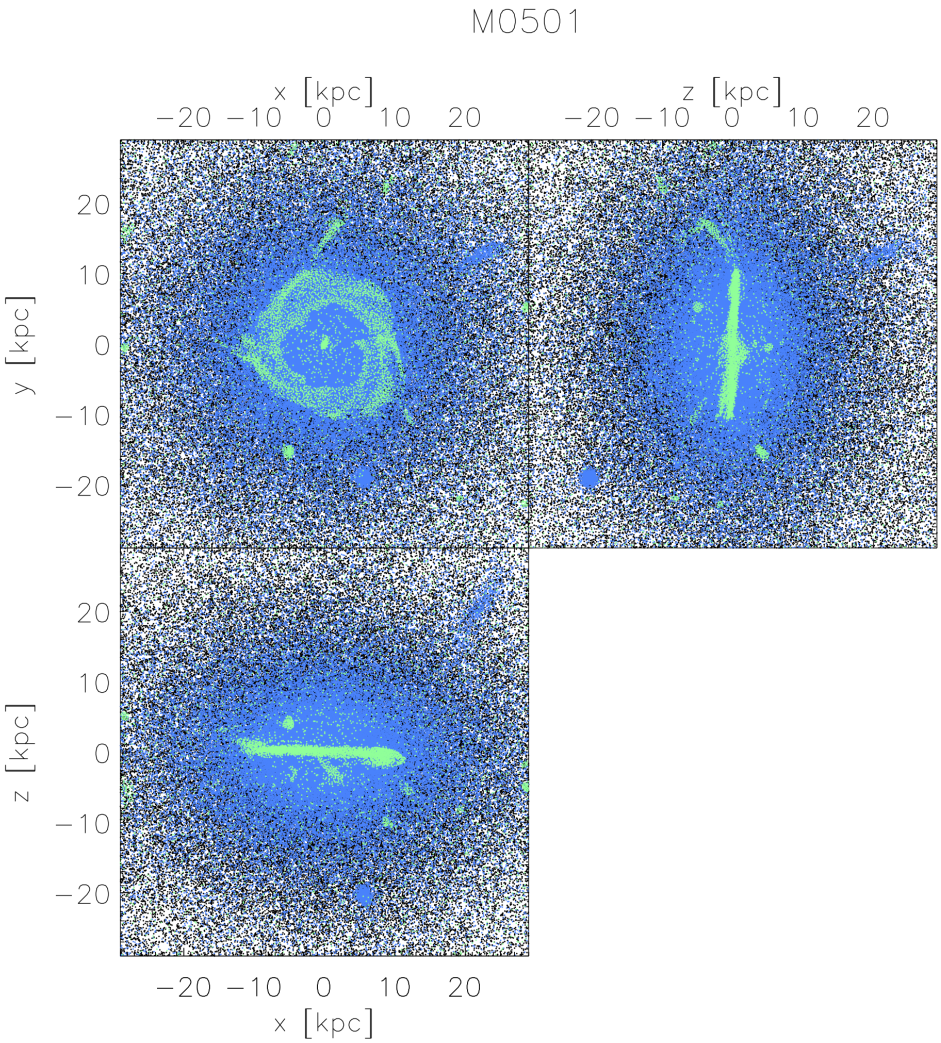

Figure 6.3: Elliptical galaxy M0501. Dark matter particles are shown in black, stellar particles in blue and gaseous particles in green.

6.2 Masses

The σ-bump is a kinematic feature in the outskirts of the galaxies. In these outer parts, the mass is not dominated by stars, but by dark matter. Therefore, I test whether there is a correlation between the position of the σ-bump and the position of the dark matter dominance.

In a first step, I examine the position of the σ-bump in more detail. For each galaxy I measure three radii:

- the starting radius r_{start} where the velocity dispersion first deviates from the power law fit

- the maximum radius r_{max} at which the deviation is largest
- the ending radius r_{end} where the velocity dispersion re-follows the power law .

These radii can be expressed in absolute values [kpc] or in galaxy specific values, in terms of the effective radius R_{eff}. In Table 6.1, I list the properties for the ellipticals.

Elliptical	r_{start} [kpc]	r_{max} [kpc]	r_{end} [kpc]	r_{start} [R_{eff}]	r_{max} [R_{eff}]	r_{end} [R_{eff}]
11 NB NG 13	4.5	9.8	15.5	0.53	1.16	1.82
11 NB OBH 13	6.5	12.8	19.5	1.06	2.08	3.17
11 NG 13	7.5	14.5	22	1.11	2.14	3.25
11 OBH 09	6	9.3	15	1.20	1.85	2.99
11 OBH 13	5.5	9.8	15.8	1.06	1.88	3.04
31 O8BH 13	5	8.2	17.2	1.95	3.20	6.72
31 OBH 09 320	5	10.1	15	0.48	0.97	1.44
31 OBH 13	5.5	12.5	23	1.05	2.39	4.41
mix 11 OBH 13	9	12.4	18	1.42	1.96	2.85
31 ASF 01	7	10.8	16	1.53	2.35	3.49

Table 6.1: Measured σ-bump radii: r_{start}, r_{max} and r_{end} in kpc and in R_{eff}.

These values can be compared to the radius where the dark matter starts to dominate over the stellar component. Two radii will be considered: the intersection point of the stellar density with the dark matter density r_ρ and the intersection point of the enclosed stellar mass with the enclosed dark matter r_{mass}. Both are measurements for the dark matter dominance, the former indicates the radius at which dark matter becomes important, the latter at which it dominates the galaxy. In Table 6.2, I list these values for all galaxies in sample P. It can now be tested whether there is a correlation between the bump

Elliptical	r_ρ [kpc]	r_{mass} [kpc]	r_ρ [R_{eff}]	r_{mass} [R_{eff}]
11 NB NG 13	4.3	8.7	0.51	1.03
11 NB OBH 13	3.5	8.6	0.57	1.40
11 NG 13	6.4	14.2	0.95	2.10
11 OBH 09	5.0	13.4	1.00	2.67
11 OBH 13	5.0	13.2	0.96	2.54
31 O8BH 13	3.5	10.3	1.37	4.02
31 OBH 09 320	9.5	23.3	0.91	2.24
31 OBH 13	4.5	11.0	0.86	2.11
mix 11 OBH 13	5.3	14.6	0.84	2.31
31 ASF 01	3.8	11.1	0.83	2.42

Table 6.2: Measured radii for dark matter dominance: r_ρ for density dominance and r_{mass} for mass dominance.

and the beginning of dark matter dominance. Figure 6.5 shows all three σ-bump radii against the starting radius of dark matter mass dominance (left panel) and dark matter density dominance (right panel). No correlation can be found between these quantities: the σ-bump radii are similar for all ellipticals, but do not depend on the starting point of dark matter dominance. It can thus be concluded that the σ-bump is not tracing the dark matter halo.

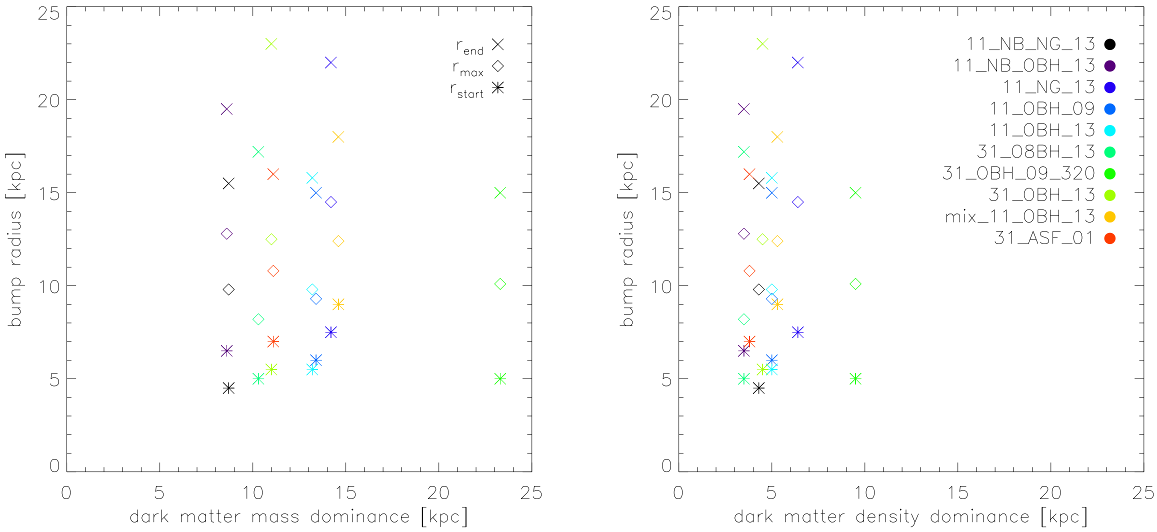

Figure 6.4: σ-bump and dark matter dominance radii. The three σ-bump radii are indicated by different symbols, the ellipticals by different colors. The left panel shows the σ-bump radii against dark matter mass dominance, the right panel against dark matter density dominance.

6.3 Components

To obtain additional information on the origin of the σ-bump one can split the intrinsic stellar velocity dispersion into components. In Figure 5.6, we already showed the line-of-sight velocity dispersion for different directions. However, this distinction does not tell much about the origin of the σ-bump, as we concluded that the σ-bump can equally be seen from all directions.

The positions and velocities of the particles can not only be analyzed in cartesian, but also in spherical coordinates. One can apply the following coordinate transformation rules on the positions,

$$r = \sqrt{x^2 + y^2 + z^2} \quad (6.1)$$

$$\theta = \arctan \frac{x^2 + y^2}{z} \quad (6.2)$$

$$\phi = \arctan \frac{y}{x} \quad (6.3)$$

and on the velocities

$$v_r = v_x \sin(\theta)\cos(\phi) + v_y \sin(\theta)\sin(\phi) + v_z \cos(\theta) \quad (6.4)$$

$$v_\theta = v_x \cos(\theta)\cos(\phi) + v_y \cos(\theta)\sin(\phi) - v_z \sin(\theta) \quad (6.5)$$

$$v_\phi = -v_x \sin(\phi) + v_y \cos(\phi). \quad (6.6)$$

The velocity dispersion can be calculated for the radial, tangential and azimuthal component separately with 5.1. The spherical components of the velocity dispersion are shown in Figure 6.5. The σ-bump is dominated by the azimuthal component and weakest in the radial component.

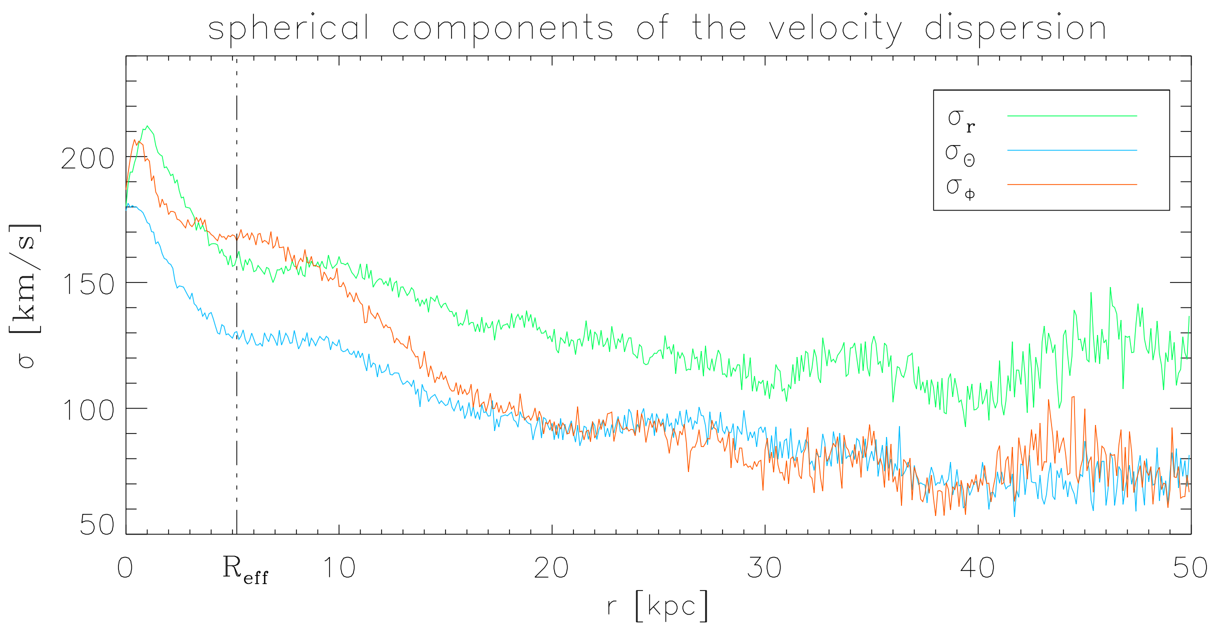

Figure 6.5: Spherical components of the velocity dispersion of 11 OBH 13. Compare Schauer et al. (2014), Figure 1, lower panel.

Besides from distinguishing the simulated particles in gas, stars and dark matter, the simulation for sample P allows a differentiation of the stellar particles in bulge, disk and stellar particles that formed in the cause of the simulation run. The σ-bump is dominated by disk particles and newly formed stars, the latter decrease quickly in density. The σ-bump might be formed through the remains of the disks of the progenitor galaxies.

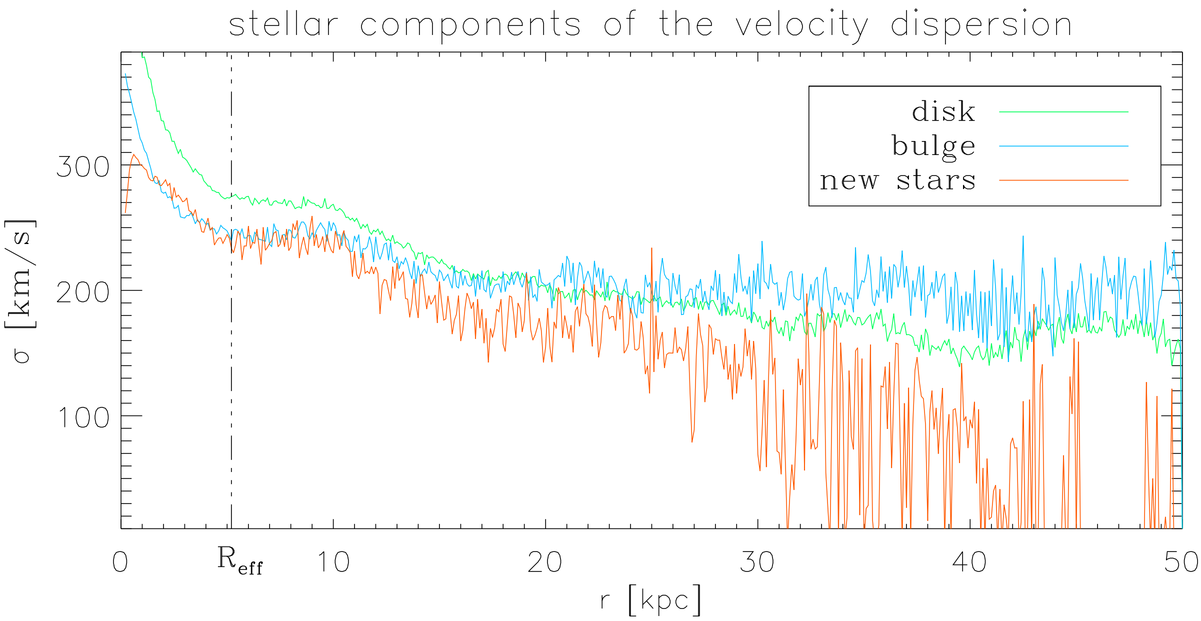

Figure 6.6: Stellar components of the velocity dispersion for 11 OBH 13: disk, bulge and in the course of the simulation newly formed stars are shown in green, blue and red.

6.4 Extreme Orbits

With the four 1:1 mass ratio simulations from sample A, different orbits are tested while keeping all other simulation parameters constant. If the σ-bump is resulting from remnants of the progenitors' disks, the interaction orbits of the setup should play an important role. Out of four tested orbits, two collide the progenitor spiral galaxies in a plane, one prograde (A03), the other retrograde (G01). The remaining two orbits align one of the galaxies perpendicular to the other, in two different rotation senses (A02 and A04).

Figure 6.7 shows the velocity dispersion of these four simulations. A σ-bump can be seen in all of them, but at smaller radii than one effective radius. The velocity dispersion is steeper for orbits in a plane than for the perpendicular progenitors, as listed in Table 6.3. In addition, the σ-bump differs: for the 90° inclined progenitors, it is more extended than for the G01 and the A03 orbit. If remnants of the progenitors' disks caused the σ-bump,

Elliptical	11 OBH 01 20 160	11 OBH A02 20 160	11 OBH A03 20 160	11 OBH A04 20 160
Slope	-0.24	-0.18	-0.26	-0.18

Table 6.3: Slopes of the power law fit to the velocity dispersion of the stellar component at 3 Gyrs for all ellipticals of sample A.

one would expect a higher velocity dispersion and maybe a more dominant σ-bump for two counterrotating disk than for two rotating disks in equal direction. But Figure 6.7 shows similar results for velocity dispersion of orbits G01 (retrograde) and A03 (prograde). Only the σ-bump is more compact for the prograde orbit. It therefore cannot be the only reason for the σ-bump.

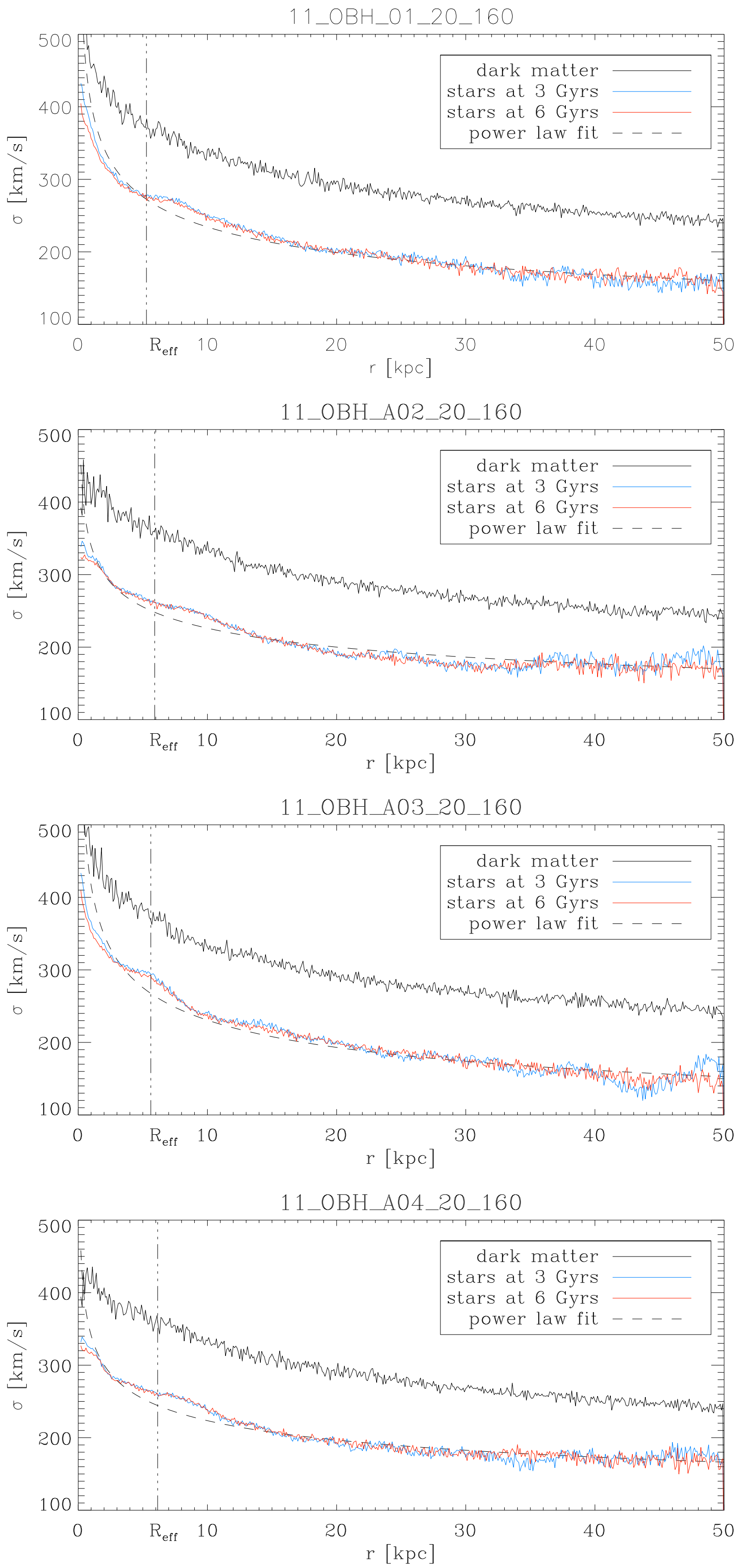

Figure 6.7: Velocity dispersion for all four 1:1 mergers in sample A.

6.5 Particle Tracers

In the major merger simulations, every particle is equipped with an ID and can therefore be traced through all snapshots. I will use this property to select particles from the 3Gyrs snapshot 149 and retrace them to the first snapshot 000. At this first snapshot, the two progenitor disk galaxies are fully separated.

Two criteria will be used for defining a σ-bump particle in the 3Gyrs snapshot:

- Radius criterion: all particles between one and two effective radii, $1R_{\mathrm{eff}} < r < 2R_{\mathrm{eff}}$
- Velocity criterion: all particles whose velocity differs more than one standard deviation from the mean velocity. Therefore, the mean velocity $< v >=< \sqrt{v_x^2 + v_y^2 + v_z^2} >$ and the standard deviation $\sigma' = \sqrt{< v^2 > - < v >^2}$ are calculated in radial bins of 0.2 kpc. For $v << v > -\sigma' \vee v >< v > +\sigma'$, the velocity criterion is fulfilled.

Figure 6.8 shows the phasespace diagram of 11 OBH 13 at 3 Gyrs, displaying velocity against radius. It is used to outline the selection criteria: all yellow particles fulfill the radius criterion, all yellow particles above or below both red lines fulfill both radius and velocity criterion.

In snapshot 000, most particles are located in the centers of the progenitor galaxies. Figure 6.9 shows stellar and σ-bump particles in the snapshot reference frame, indicated by different colors. It seems reasonable that this feature which extends to two R_{eff} is produced by the inner parts of the progenitor galaxies. In this figure, particles with the radius criterion show a similar distibution as particles with radius and velocity criteria. In the following, I name the galaxy on the right with positive x-values 'galaxy 1', the galaxy on the left with negative x-values 'galaxy 2'.

In addition, Figure 6.10 shows the phasespace diagrams of the σ-bump particles of the progenitors in snapshot 000. Galaxy memberships and the two σ-bump criteria are displayed in different colors. One can see that galaxy 1 contributes more central particles to the σ-bump, but the two criteria do not reveal a difference.

Histogram 6.11 strengthens this hypothesis. The σ-bump is equally produced by particles of the two galaxies, the particles show a similar distribution around a radius of 5kpc. There is a slight difference, the σ-bump particles lie more central in galaxy 2 than in galaxy 1.

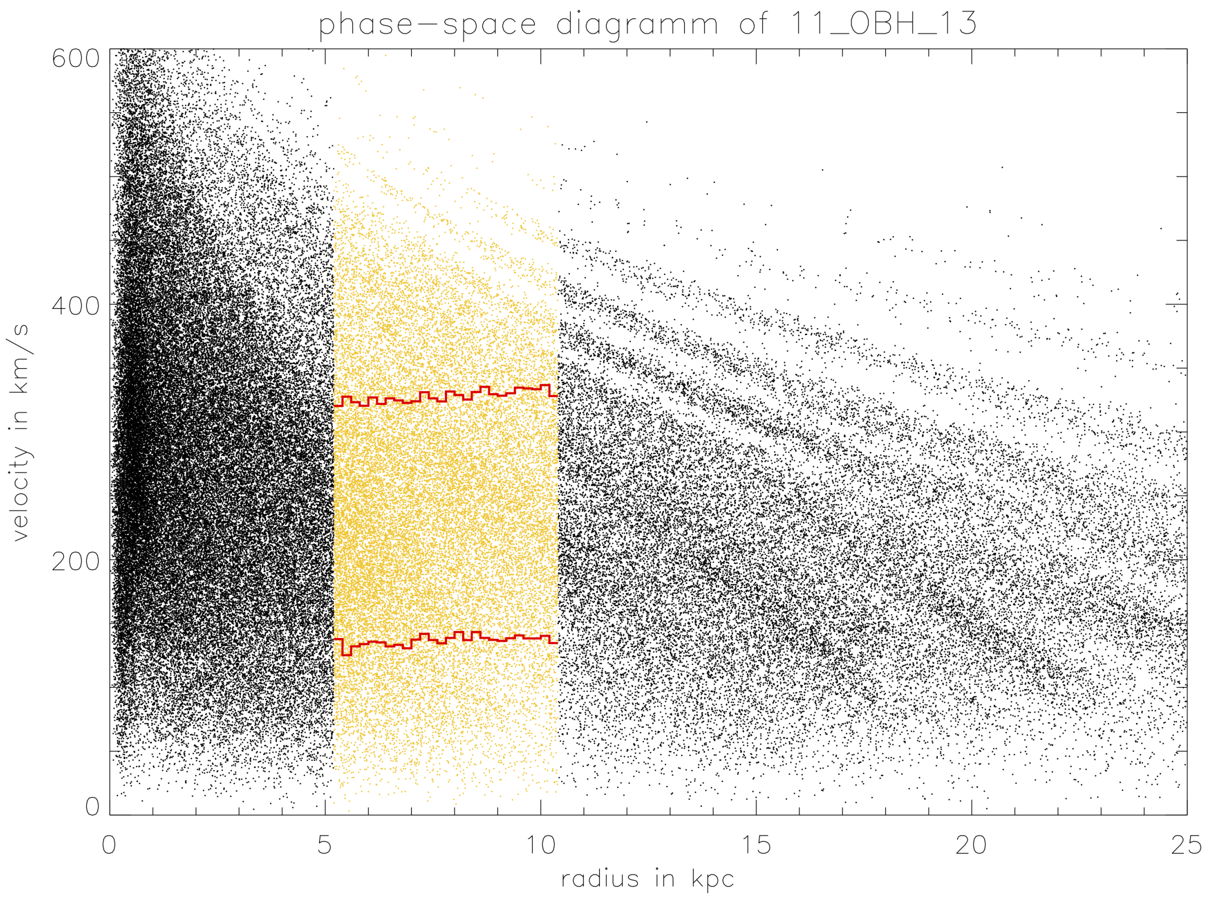

Figure 6.8: Phasespace diagram for 11 OBH 13 at 3 Gyrs. The σ-bump selection criteria are shown: the radius criteron (yellow particles) and the radius and velocity criterion (yellow particles above or below both red lines). For clarity, every 5th stellar particle is shown.

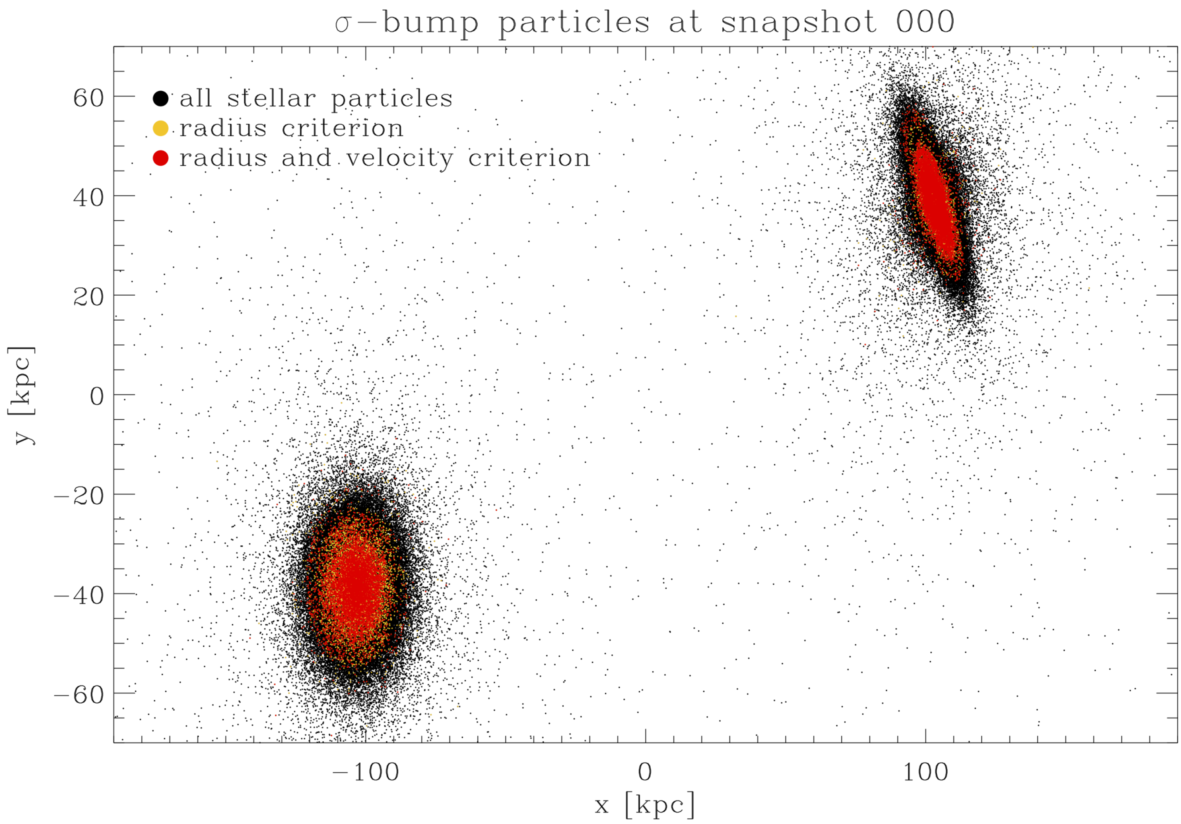

Figure 6.9: Stellar and σ-bump particles in snapshot 000 of 11 OBH 13. This figure shows stellar particles (black) of the progenitor galaxies on their parabolic orbit. σ-bump particles with radius criterion (yellow) and radius and velocity criterion (red) are shown in color.

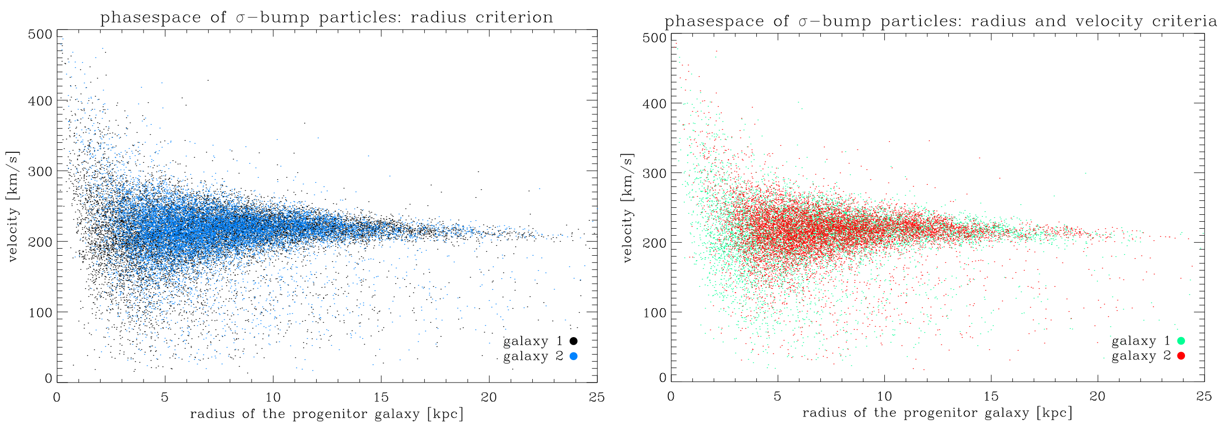

Figure 6.10: Phasespace diagrams forσ-bump particles in snapshot 000 of 11 OBH 13.

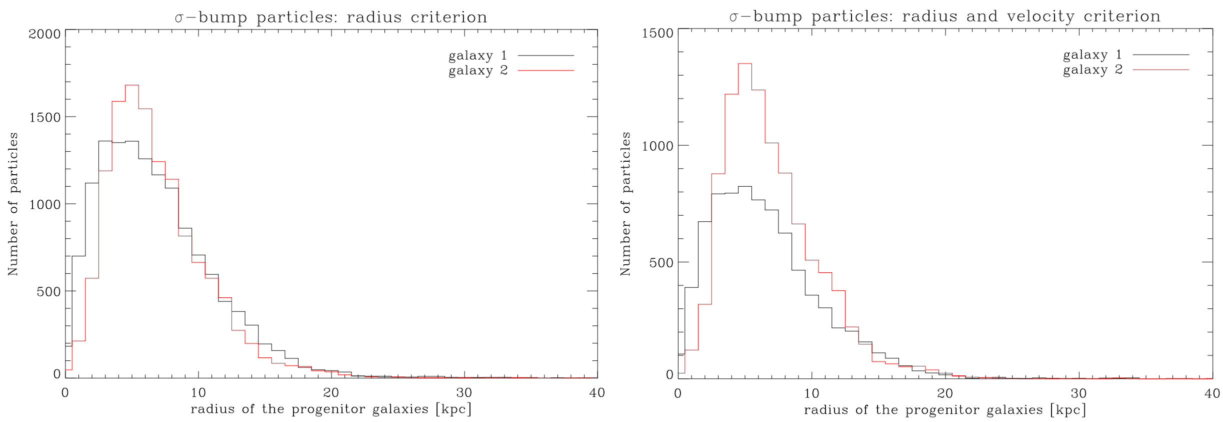

Figure 6.11: Radial histograms for σ-bump particles in snapshot 000

7 Conclusion

I still have to write this chapter.

Bibliography

Arnold, J. A., Romanowsky, A. J., Brodie, J. P., Chomiuk, L., Spitler, L. R., Strader, J., Benson, A. J., & Forbes, D. A. 2011, The Astrophysical Journal, Letters, 736, L26

Bertschinger, E. 1995, ArXiv Astrophysics e-prints

Binney, J. J., Davies, R. L., & Illingworth, G. D. 1990, The Astrophysical Journal, 361, 78

Bois, M., Bournaud, F., Emsellem, E., Alatalo, K., Blitz, L., Bureau, M., Cappellari, M., Davies, R. L., Davis, T. A., de Zeeuw, P. T., Duc, P.-A., Khochfar, S., Krajnović, D., Kuntschner, H., Lablanche, P.-Y., McDermid, R. M., Morganti, R., Naab, T., Oosterloo, T., Sarzi, M., Scott, N., Serra, P., Weijmans, A., & Young, L. M. 2010, Monthly Notices of the Royal Astronomical Society, 406, 2405

Bois, M., Emsellem, E., Bournaud, F., Alatalo, K., Blitz, L., Bureau, M., Cappellari, M., Davies, R. L., Davis, T. A., de Zeeuw, P. T., Duc, P.-A., Khochfar, S., Krajnović, D., Kuntschner, H., Lablanche, P.-Y., McDermid, R. M., Morganti, R., Naab, T., Oosterloo, T., Sarzi, M., Scott, N., Serra, P., Weijmans, A.-M., & Young, L. M. 2011, Monthly Notices of the Royal Astronomical Society, 416, 1654

Burkert, A., Naab, T., Johansson, P. H., & Jesseit, R. 2008, The Astrophysical Journal, 685, 897

Cappellari, M., Emsellem, E., Krajnović, D., McDermid, R. M., Scott, N., Verdoes Kleijn, G. A., Young, L. M., Alatalo, K., Bacon, R., Blitz, L., Bois, M., Bournaud, F., Bureau, M., Davies, R. L., Davis, T. A., de Zeeuw, P. T., Duc, P.-A., Khochfar, S., Kuntschner, H., Lablanche, P.-Y., Morganti, R., Naab, T., Oosterloo, T., Sarzi, M., Serra, P., & Weijmans, A.-M. 2011, Monthly Notices of the Royal Astronomical Society, 413, 813

Carter, D. 1987, The Astrophysical Journal, 312, 514

Coccato, L., Arnaboldi, M., Capaccioli, M., Cortesi, A., De Lorenzi, F., Douglas, N., Freeman, K., Gerhard, O., Kuijken, K., Merrifield, M., Napolitano, R., Romanowsky, A., & Ventimiglia, G. 2012, in IAC Talks, Astronomy and Astrophysics Seminars from the Instituto de Astrofísica de Canarias, 301

Coccato, L., Gerhard, O., Arnaboldi, M., Das, P., Douglas, N. G., Kuijken, K., Merrifield, M. R., Napolitano, N. R., Noordermeer, E., Romanowsky, A. J., Capaccioli, M., Cortesi, A., de Lorenzi, F., & Freeman, K. C. 2009, Monthly Notices of the Royal Astronomical Society, 394, 1249

Cooper, A. P., Martínez-Delgado, D., Helly, J., Frenk, C., Cole, S., Crawford, K., Zibetti, S., Carballo-Bello, J. A., & GaBany, R. J. 2011, The Astrophysical Journal, Letters, 743, L21

de Vaucouleurs, G. 1953, Monthly Notices of the Royal Astronomical Society, 113, 134

Dopita, M. A., Jacoby, G. H., & Vassiliadis, E. 1992, The Astrophysical Journal, 389, 27

Douglas, N. G., Arnaboldi, M., Freeman, K. C., Kuijken, K., Merrifield, M. R., Romanowsky, A. J., Taylor, K., Capaccioli, M., Axelrod, T., Gilmozzi, R., Hart, J., Bloxham, G., & Jones, D. 2002, Publications of the Astronomical Society of the Pacific, 114, 1234

Douglas, N. G., Napolitano, N. R., Romanowsky, A. J., Coccato, L., Kuijken, K., Merrifield, M. R., Arnaboldi, M., Gerhard, O., Freeman, K. C., Merrett, H. R., Noordermeer, E., & Capaccioli, M. 2007, The Astrophysical Journal, 664, 257

Emsellem, E., Cappellari, M., Krajnović, D., Alatalo, K., Blitz, L., Bois, M., Bournaud, F., Bureau, M., Davies, R. L., Davis, T. A., de Zeeuw, P. T., Khochfar, S., Kuntschner, H., Lablanche, P.-Y., McDermid, R. M., Morganti, R., Naab, T., Oosterloo, T., Sarzi, M., Scott, N., Serra, P., van de Ven, G., Weijmans, A.-M., & Young, L. M. 2011, Monthly Notices of the Royal Astronomical Society, 414, 888

Emsellem, E., Cappellari, M., Krajnović, D., van de Ven, G., Bacon, R., Bureau, M., Davies, R. L., de Zeeuw, P. T., Falcón-Barroso, J., Kuntschner, H., McDermid, R., Peletier, R. F., & Sarzi, M. 2007, Monthly Notices of the Royal Astronomical Society, 379, 401

Forestell, A. D. & Gebhardt, K. 2010, The Astrophysical Journal, 716, 370

Foster, C., Spitler, L. R., Romanowsky, A. J., Forbes, D. A., Pota, V., Bekki, K., Strader, J., Proctor, R. N., Arnold, J. A., & Brodie, J. P. 2011, Monthly Notices of the Royal Astronomical Society, 415, 3393

Fried, J. W. & Illingworth, G. D. 1994, The Astronomical Journal, 107, 992

Goudfrooij, P., Hansen, L., Jorgensen, H. E., Norgaard-Nielsen, H. U., de Jong, T., & van den Hoek, L. B. 1994, Astronomy & Astrophysics, Supplement, 104, 179

Hernquist, L. 1990, The Astrophysical Journal, 356, 359

Hubble, E. P. 1936, Realm of the Nebulae (New Haven: Yale University Press)

Johansson, P. H., Burkert, A., & Naab, T. 2009a, The Astrophysical Journal, Letters, 707, L184

Johansson, P. H. & Efstathiou, G. 2006, Monthly Notices of the Royal Astronomical Society, 371, 1519

Johansson, P. H., Naab, T., & Burkert, A. 2009b, The Astrophysical Journal, 690, 802

Jorgensen, I., Franx, M., & Kjaergaard, P. 1996, Monthly Notices of the Royal Astronomical Society, 280, 167

Kim, D. & Im, M. 2013, The Astrophysical Journal, 766, 109

Krajnović, D., Emsellem, E., Cappellari, M., Alatalo, K., Blitz, L., Bois, M., Bournaud, F., Bureau, M., Davies, R. L., Davis, T. A., de Zeeuw, P. T., Khochfar, S., Kuntschner, H., Lablanche, P.-Y., McDermid, R. M., Morganti, R., Naab, T., Oosterloo, T., Sarzi, M., Scott, N., Serra, P., Weijmans, A.-M., & Young, L. M. 2011, Monthly Notices of the Royal Astronomical Society, 414, 2923

Lambas, D. G., Alonso, S., Mesa, V., & O'Mill, A. L. 2012, Astronomy & Astrophysics, 539, A45

McKee, C. F. & Ostriker, J. P. 1977, The Astrophysical Journal, 218, 148

Méndez, R. H., Riffeser, A., Kudritzki, R.-P., Matthias, M., Freeman, K. C., Arnaboldi, M., Capaccioli, M., & Gerhard, O. E. 2001, The Astrophysical Journal, 563, 135

Méndez, R. H., Teodorescu, A. M., & Kudritzki, R.-P. 2008, The Astrophysical Journal, Supplement, 175, 522

Méndez, R. H., Teodorescu, A. M., Kudritzki, R.-P., & Burkert, A. 2009, The Astrophysical Journal, 691, 228

Merrett, H. R., Merrifield, M. R., Douglas, N. G., Kuijken, K., Romanowsky, A. J., Napolitano, N. R., Arnaboldi, M., Capaccioli, M., Freeman, K. C., Gerhard, O., Coccato, L., Carter, D., Evans, N. W., Wilkinson, M. I., Halliday, C., & Bridges, T. J. 2006, Monthly Notices of the Royal Astronomical Society, 369, 120

Mo, H. J., Mao, S., & White, S. D. M. 1998, Monthly Notices of the Royal Astronomical Society, 295, 319

Naab, T. & Burkert, A. 2003, The Astrophysical Journal, 597, 893

Napolitano, N. R., Romanowsky, A. J., Capaccioli, M., Douglas, N. G., Arnaboldi, M., Coccato, L., Gerhard, O., Kuijken, K., Merrifield, M. R., Bamford, S. P., Cortesi, A., Das, P., & Freeman, K. C. 2011, Monthly Notices of the Royal Astronomical Society, 411, 2035

Napolitano, N. R., Romanowsky, A. J., Coccato, L., Capaccioli, M., Douglas, N. G., Noordermeer, E., Gerhard, O., Arnaboldi, M., de Lorenzi, F., Kuijken, K., Merrifield, M. R., O'Sullivan, E., Cortesi, A., Das, P., & Freeman, K. C. 2009, Monthly Notices of the Royal Astronomical Society, 393, 329

Navarro, J. F., Frenk, C. S., & White, S. D. M. 1997, The Astrophysical Journal, 490, 493

Norris, M. A., Sharples, R. M., & Kuntschner, H. 2006, Monthly Notices of the Royal Astronomical Society, 367, 815

Oser, L., Ostriker, J. P., Naab, T., Johansson, P. H., & Burkert, A. 2010, The Astrophysical Journal, 725, 2312

Paudel, S., Lisker, T., Hansson, K. S. A., & Huxor, A. P. 2014, Monthly Notices of the Royal Astronomical Society, 443, 446

Pota, V., Forbes, D. A., Romanowsky, A. J., Brodie, J. P., Spitler, L. R., Strader, J., Foster, C., Arnold, J. A., Benson, A., Blom, C., Hargis, J. R., Rhode, K. L., & Usher, C. 2013, Monthly Notices of the Royal Astronomical Society, 428, 389

Power, C., Navarro, J. F., Jenkins, A., Frenk, C. S., White, S. D. M., Springel, V., Stadel, J., & Quinn, T. 2003, Monthly Notices of the Royal Astronomical Society, 338, 14

Proctor, R. N., Forbes, D. A., Romanowsky, A. J., Brodie, J. P., Strader, J., Spolaor, M., Mendel, J. T., & Spitler, L. 2009, Monthly Notices of the Royal Astronomical Society, 398, 91

Remus, R.-S., Burkert, A., Dolag, K., Johansson, P. H., Naab, T., Oser, L., & Thomas, J. 2013, The Astrophysical Journal, 766, 71

Renzini, A. 2006, Annual Review of Astronomy & Astrophysics, 44, 141

Romanowsky, A. J., Douglas, N. G., Arnaboldi, M., Kuijken, K., Merrifield, M. R., Napolitano, N. R., Capaccioli, M., & Freeman, K. C. 2003, Science, 301, 1696

Romanowsky, A. J. & Fall, S. M. 2012, The Astrophysical Journal, Supplement, 203, 17

Sambhus, N., Gerhard, O., & Méndez, R. H. 2006, The Astronomical Journal, 131, 837

Schauer, A. T. P., Remus, R.-S., Burkert, A., & Johansson, P. H. 2014, The Astrophysical Journal, Letters, 783, L32

Schuberth, Y., Richtler, T., Hilker, M., Dirsch, B., Bassino, L. P., Romanowsky, A. J., & Infante, L. 2010, Astronomy & Astrophysics, 513, A52

Schweizer, F. 1986, Science, 231, 227

Shih, H.-Y. & Méndez, R. H. 2010, The Astrophysical Journal, Letters, 725, L97

Spergel, D. N., Bean, R., Doré, O., Nolta, M. R., Bennett, C. L., Dunkley, J., Hinshaw, G., Jarosik, N., Komatsu, E., Page, L., Peiris, H. V., Verde, L., Halpern, M., Hill, R. S., Kogut, A., Limon, M., Meyer, S. S., Odegard, N., Tucker, G. S., Weiland, J. L., Wollack, E., & Wright, E. L. 2007, The Astrophysical Journal, Supplement, 170, 377

Spergel, D. N., Verde, L., Peiris, H. V., Komatsu, E., Nolta, M. R., Bennett, C. L., Halpern, M., Hinshaw, G., Jarosik, N., Kogut, A., Limon, M., Meyer, S. S., Page, L., Tucker, G. S., Weiland, J. L., Wollack, E., & Wright, E. L. 2003, The Astrophysical Journal, Supplement, 148, 175

Springel, V. 2005, Monthly Notices of the Royal Astronomical Society, 364, 1105

Springel, V., Di Matteo, T., & Hernquist, L. 2005, Monthly Notices of the Royal Astronomical Society, 361, 776

Springel, V. & Hernquist, L. 2003, Monthly Notices of the Royal Astronomical Society, 339, 289

Strader, J., Romanowsky, A. J., Brodie, J. P., Spitler, L. R., Beasley, M. A., Arnold, J. A., Tamura, N., Sharples, R. M., & Arimoto, N. 2011, The Astrophysical Journal, Supplement, 197, 33

Toomre, A. & Toomre, J. 1972, The Astrophysical Journal, 178, 623

Tremaine, S., Gebhardt, K., Bender, R., Bower, G., Dressler, A., Faber, S. M., Filippenko, A. V., Green, R., Grillmair, C., Ho, L. C., Kormendy, J., Lauer, T. R., Magorrian, J., Pinkney, J., & Richstone, D. 2002, The Astrophysical Journal, 574, 740

van Albada, T. S., Bahcall, J. N., Begeman, K., & Sancisi, R. 1985, The Astrophysical Journal, 295, 305

van der Marel, R. P. & Franx, M. 1993, The Astrophysical Journal, 407, 525